Growth Mechanism, Kinetics and Morphology of Gas Hydrates of Carbon Dioxide, Methane and their Mixtures

Mécanisme de croissance, cinétique et morphologie des hydrates gazeux de dioxyde de carbone, de méthane et de leurs mélanges

A Thesis Submitted to the Division of Graduate Studies

of the Royal Military College of Canada

by

Camilo Martínez

Department of Chemistry and Chemical Engineering

In partial Fulfillment of the Requirements for the Degree of

Master of Applied Science

August, 2021

Acknowledgments

I would like to thank my parents, Carlos and Mónica, for their love and support through the years. To my family in Colombia for whom the distance was not an obstacle for them to show their love. To Camila for being there as my partner, my friend and my confidant. To Sebastián and Andrés for being amazing friends and housemates. To Dr. Juan Beltran, for his dedication, patience, mentoring, for being a true example of what a great academic, engineer and person is. To all my Kingston friends, who have become my family. To the staff at the Department of Chemical Engineering and Chemistry at the RMC. To everyone who has contributed towards my personal and professional growth.

Thanks to the Natural Sciences and Engineering Research Council of Canada (NSERC), the Canadian Foundation for Innovation (CFI), the Royal Military College of Canada Short Term Research Needs Program, the Royal Military College of Canada COVID Relief Funds, the Royal Military College of Canada ARP and Ingeniería de Proyectos SAS whose funding made this project possible.

Abstract

Morphology, film growth rate and growth mechanism of gas hydrates of methane, carbon dioxide and two of their mixtures (CH4+CO2, 80:20 and 30:70 nominal concentration) were studied using the 3-in-1 technique. Hydrates of carbon dioxide, methane and the two mixtures presented euhedral, faceted crystal habits at low driving forces. As growth rates increased, carbon dioxide and 30:70 formed different spherulitic morphologies while methane and the 80:20 mixture exhibited granular and smooth spherulites. These results solve previous apparent contradictions in literature about the morphology of hydrates of methane, carbon dioxide and their mixtures. It was also shown that hydrate growth of methane, carbon dioxide and their mixtures proceeds via partial dissociation of the growing crystal. The single-guest, mass-transfer model proposed by Kishimoto & Ohmura (2012) was extended to binary guest systems. At low driving forces, our extended model related morphology and growth rates with the mass-transfer driving force. Furthermore, it was shown that the model could be correlated to an abrupt change in morphology common to all systems. This change in morphology was explained by a shift in the crystal growth mechanism. At higher driving forces, growth rates and morphologies were different for all systems.

Résumé

La morphologie, la vitesse de croissance du film et le mécanisme de croissance des hydrates de gaz de méthane, de dioxyde de carbone et de deux de leurs mélanges (CH4 + CO2, concentration nominale 80:20 et 30:70) ont été étudiés en utilisant la technique 3-en-1. Les hydrates de dioxyde de carbone, de méthane et des deux mélanges ont présenté des habitudes cristallines à facettes euédriques à de faibles forces d'entrainement. À mesure que les taux de croissance augmentaient, le dioxyde de carbone et le mélange 30:70 formaient différentes morphologies sphérolitiques tandis que le méthane et le mélange 80:20 présentaient des sphérulites granulaires et lisses. Ces résultats résolvent des contradictions apparentes antérieures dans la littérature sur la morphologie des hydrates de méthane, de dioxyde de carbone et de leurs mélanges. Il a également été démontré que la croissance des hydrates de méthane, de dioxyde de carbone et de leurs mélanges se fait par dissociation partielle du cristal en croissance. Le modèle de transfert de masse à invité unique, proposé par Kishimoto & Ohmura (2012), a été étendu aux systèmes à invités binaires. À faibles forces motrices, notre modèle étendu a associé la morphologie et les taux de croissance à la force motrice de transfert de masse. De plus, il a été démontré que le modèle pouvait être corrélé à un changement drastique de morphologie, commune à tous les systèmes. Ce changement de morphologie s'explique par un changement dans le mécanisme de croissance cristalline. À des forces motrices plus élevées, les taux de croissance et les morphologies se sont avérés différents pour tous les systèmes.

Contents

Nomenclature

Greek Letters

Δ	Difference
μ	Chemical potential
ν	Stoichiometric coefficient
π	Number of phases

Subscripts and Abbreviations

eq	Equilibrium
exp	Experimental
HI	Hydrate Ice
HL	Hydrate Liquid
HLV	Hydrate Liquid Vapor
HVI	Hydrate Vapor Ice
i	Guest i, CH_4, CO_2
IHL	Ice Hydrate Liquid
IV	Ice Vapor
LV	Liquid Vapor

Variables

$\dot{m}$	Molar flux
A	Avogadro number
a	Lattice constant
F	Degrees of freedom
f	Fugacity
g	Hydrate guest
H	Henry's constant
h	Mass-transfer coefficient
k	Boltzmann Constant
M	Molar mass
N	Number of components in a system
n	Hydration number
P	Pressure
r	Radius
T	Temperature
t	Time
V	Volume
v	Velocity
x	Liquid-phase composition
y	Vapor phase composition

List of Figures

List of Tables

Preface

Gas hydrates are crystalline, non-stoichiometric compounds that form when volatile guests come into contact with water at the appropriate conditions (generally, above atmospheric pressure and temperatures under 8° C) (Koh *et al.*, 2011). Gas hydrates were first discovered in 1810 by Davy while experimenting with chlorine gas (Davy, 1811). Hammerschmidt (1934) discovered the role of gas hydrates in plugging oil and gas pipelines. Following this discovery, research into plug mitigation via additives was the center of hydrate research (Perrin *et al.*, 2013; Sum *et al.*, 2012). Makogon published the discovery of *in-situ* gas hydrate in 1965 (Englezos, 1993b). The discovery of natural gas hydrate bearings opened the possibility of exploiting natural gas from hydrates. It was projected that there is twice the energy available in hydrates bearings than all other fossil fuels combined (Katz, 1971). Other applications of gas hydrate technologies include natural gas and hydrogen storage, carbon dioxide sequestration, desalinization of water and management of flue gases Koh *et al.* (2011); Kang & Lee (2000). Gas hydrates can store 164 times the volume of the guest substance at standard pressure and temperature Koh *et al.* (2011).

Methane and carbon dioxide are essential for hydrate research for various reasons. These two gases are the most common anthropogenic greenhouse gases emitted. Methane is the main component of natural gas, with small fractions of carbon dioxide been found on natural gas exploited in different parts of the world (Gong *et al.*, 2014; Kidnay, 2020). Gas hydrates formed by methane are the most common in natural sediments (Lu *et al.*, 2007). Injection of carbon dioxide on natural hydrate sediments was proposed as a method of exploiting natural gas (B. P. McGrail, 2007).

The morphology (i.e., how gas hydrates *look*) of methane and carbon dioxide hydrates have been widely studied with apparent contradictions in their results. Servio & Englezos (2003) observed similar jagged morphology for both gases. Several authors have published studies showing differences in the morphology of methane and carbon dioxide (Ohmura *et al.*, 2004, 2005; Beltran & Servio, 2010; Decarie & Beltran,

2011; Uchida *et al.*, 1999). Studies using mixtures of methane and carbon dioxide also presented apparent discrepancies on the effect of composition on morphology. Daniel-David *et al.* (2015) stated that the composition of the vapor phase does have an effect on the morphology of mixed hydrates while Ueno *et al.* (2015) found that composition of the feed gas did not affect morphology.

Studies in the Beltran Hydrate Research Group aimed to further study the morphology of methane and carbon dioxide. Decarie (2012) found significant differences in the morphology of carbon dioxide and methane with and without previous formation history. Duquesnay *et al.* (2016) developed a 3-in-1 reactor that allowed high-resolution imaging and tight temperature and pressure control. Sandoval (2015) used this novel 3-in-1 and found differences in the morphology of carbon dioxide and methane at the different experimental conditions used. Ortiz (2018) studied two mixtures of methane and carbon dioxide along with the pure gases. An effect of the vapor composition on morphology was observed along with different morphology for methane, carbon dioxide and the two mixtures studied. All these studies used a heat-transfer limited driving force to study and classify morphology. There are some indications in the literature that hydrate growth is a mass-transfer limited process Kishimoto & Ohmura (2012); Saito *et al.* (2010); Ohmura *et al.* (2004).

This study aims to apply the 3-in-1 technique to study morphology, growth velocities and growth mechanism of methane, carbon dioxide and two mixtures using a mass-transfer limited driving force. Morphology and growth rate data from Sandoval (2015) and Ortiz (2018) were used in this study. This document is divided in four sections: (1) Background, where basic knowledge of gas hydrates is presented together with a survey of the literature and of relevant unpublished work in the Beltran lab; (2) Experimental, where the apparatus unique techniques and a new model for driving force is described; (3) Results and Discussion are presented in a combined format for ease of analysis; (4) Conclusions, which offer a general summary and propose directions for future work.

Chapter 1

Background

1.1 Gas Hydrates

Gas hydrates are inclusion compounds that form when a volatile guest molecule is in contact with water at moderate pressures ($P > 2$ MPa) and low temperatures ($T < 8^{\circ}$ C). Some of the most common hydrate guests are light hydrocarbons (Methane, ethane, propane) and carbon dioxide. Other hydrates formers include hydrogen sulfide, xenon and tetrahydrofuran (Sloan & Koh, 2008).

Hydrates are solids with approximately an 85% molar composition of water and thus some similarities with ice are shared. Physical appearance, refractive index and density are some of the properties shared between hydrates and ice. Other properties like heat capacity, thermal conductivity and mechanical strength differ significantly between hydrates and ice (Sloan & Koh, 2008).

1.1.1 Crystalline Structure

Gas hydrates have three common crystalline structures, structure I (sI), structure II (sII) and structure H (sH), as seen on Figure 1.1. The structure formed depends on the size of the guest molecule.(Koh *et al.*, 2011) For example, CH_4 and CO_2 are sI formers while C_3H_8 is a sII former. Pentagonal dodecahedral cages (5^{12} on Figure 1.1) are the basic building structure for all common cubic hydrate structures. Structure I also includes tetrakaidecahedral cages ($5^{12}6^2$ on Figure 1.1). (Mak & McMullan, 1965) Structure II is formed by 5^{12} cages along with a larger $5^{12}6^4$ cage. Structure H is formed in specific cases for mixtures with small and big guest molecules, for example methane and neohexane.(Sloan & Koh, 2008) Structure H is stabilized

by 3 types of cages: a small cage (5^{12}), medium cage ($4^3 5^6 6^3$) and a large icosahedral cage ($5^{12}6^8$).

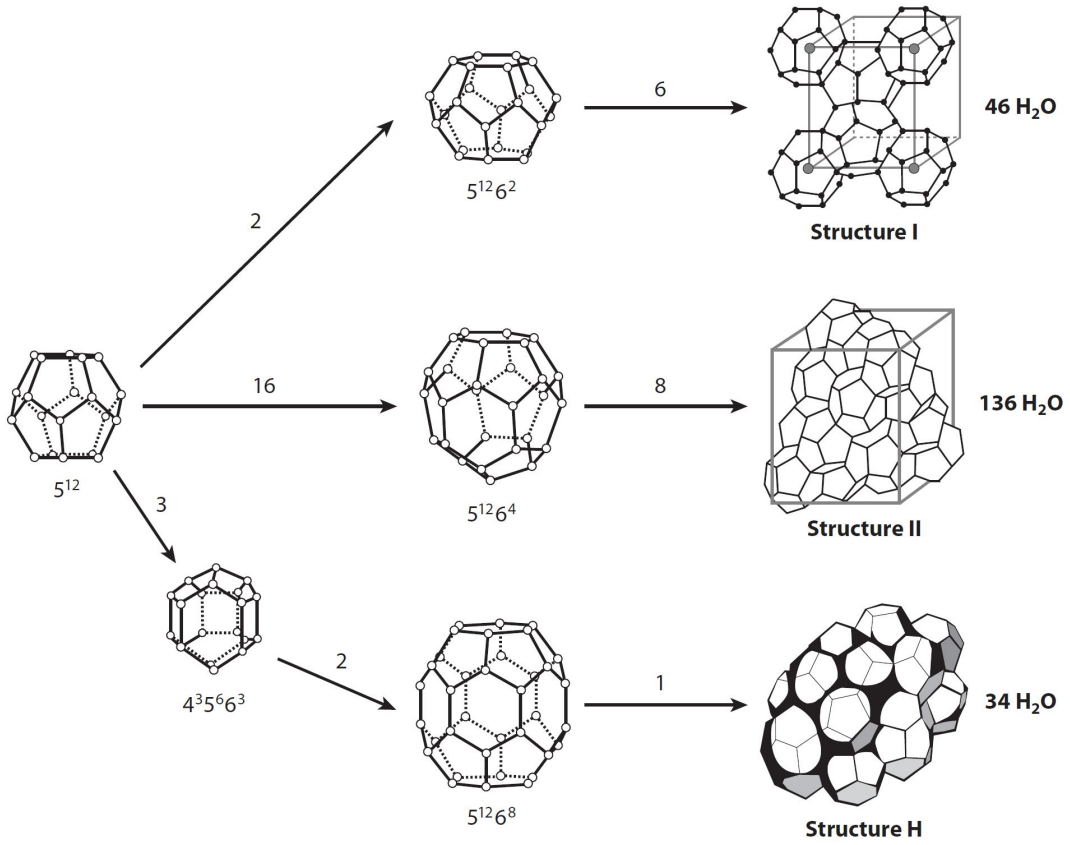

Figure 1.1: Common cubic crystalline structures of gas hydrates. Base number indicated vertices of a face, exponent indicates number of faces i.e $5^{12}6^2$ has 12 pentagonal faces and 2 hexagonal faces. Numbers above the lines indicate the number of cages of each size in the structure (i.e structure I has 2 5^{12} cages and 6 $5^{12}6^2$ cages). Reproduced from Koh *et al.* (2011) (with permission).

1.2 Phase Equilibria

A non-reacting system at equilibrium is characterized by a set number of intensive variables. The number of intensive variables is given by the Gibbs Phase Rule:

$$F = 2 + N - \pi \tag{1.1}$$

Where F is the degrees of freedom (intensive variables), N is the number of components in the system and π is the number of phases (Smith *et al.*, 2001). Applied to hydrates, with a pure feed gas (N = 2, π =

3) the degrees of freedom are equal to 1. To properly present the hydrate-liquid-vapor (HLV) equilibrium for a single-guest system, one intensive variable must be controlled while reporting another one (F+1). An example of this is in Figure 1.2, where pressure and temperature are shown for a methane-water system (Beltran *et al.*, 2012). Hydrate forming systems with binary mixtures have 2 degrees of freedom under HLV (N = 3, π = 3). Along with temperature and pressure, composition needs to be specified on an HLV graph for these systems.

1.2.1 Hydrate Forming Region

A partial phase diagram for a methane-water system can be seen on Figure 1.2. The blue line represents the hydrate-liquid-vapor (HLV) equilibrium for methane hydrates. At higher pressures and lower temperatures than this line, methane hydrates will form. At lower pressures and higher temperatures than the HLV line, hydrates will dissociate.

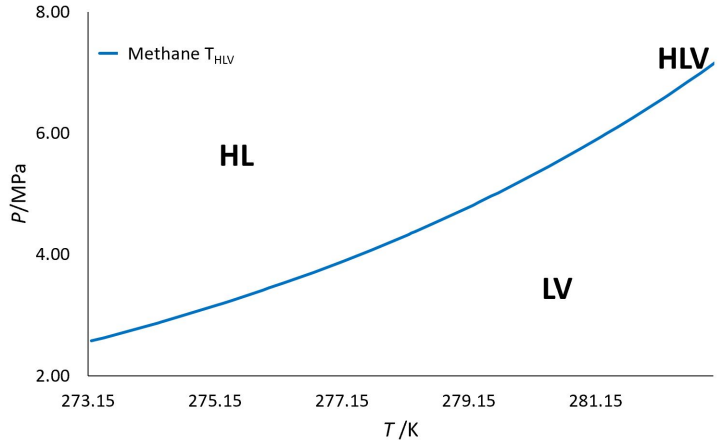

Figure 1.2: Partial phase diagram for methane+water system. Blue line represent hydrate-liquid vapor equilibrium conditions. HL, Hydrate-liquid region. HLV, hydrate-liquid-vapor equilibrium. LV, liquid-vapor

1.2.1.1 Hydrate-Liquid-Vapor Equilibrium

Gas hydrates formed by CO_2, CH_4 and their mixtures have different hydrate-liquid-vapor equilibrium conditions. Carbon dioxide hydrates are stable at lower pressures and higher temperatures than CH_4, as seen on Figure 1.3. Hydrate-liquid-vapor equilibrium of CH_4+CO_2 mixtures will be found at conditions in between the single guest hydrates. Figure 1.4 shows that as CO_2 content increases at a constant temperature, equilibrium pressure decreases.

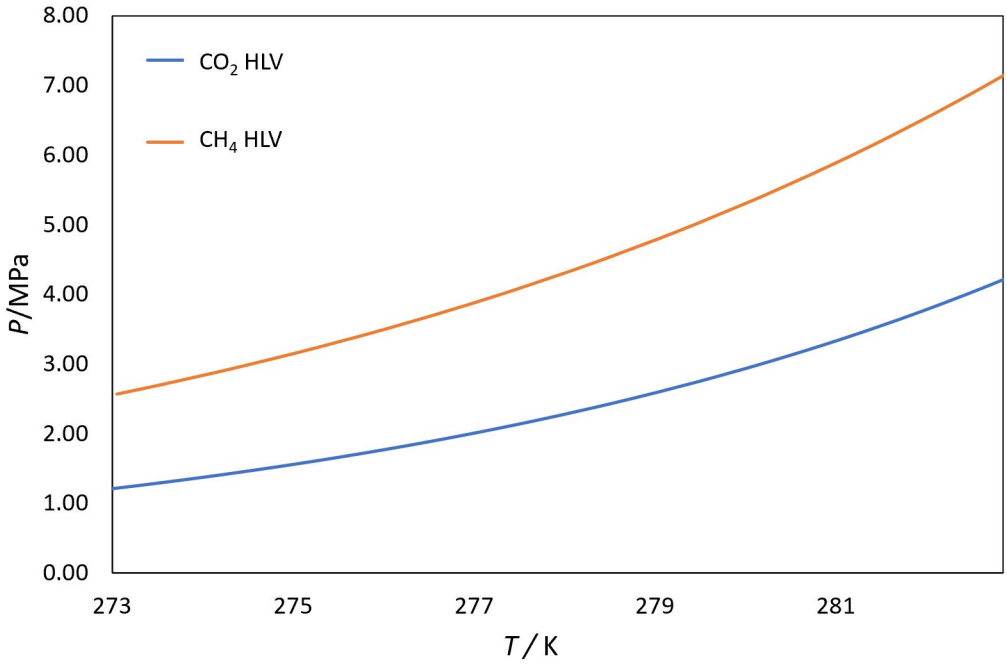

Figure 1.3: Pressure vs temperature diagram. Blue line corresponds to methane HLV equilibrium, orange to carbon dioxide hydrate HLV equilibrium. HLV conditions calculated using Herriot Watt University's HWPVT Software.

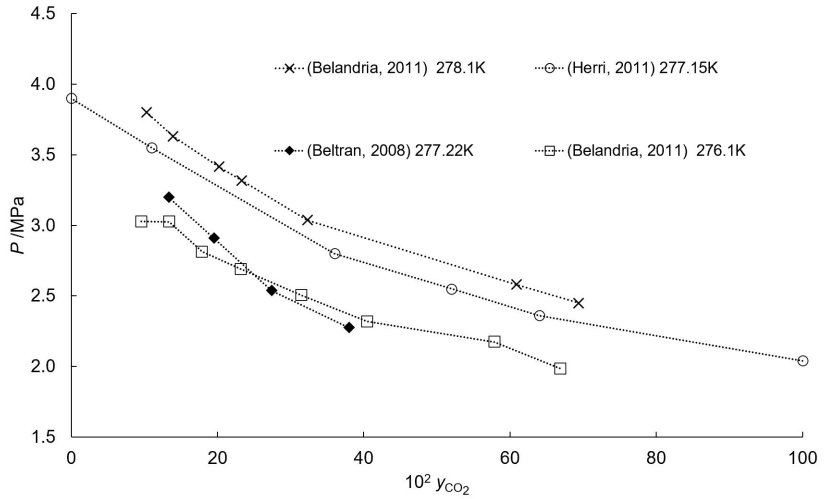

Figure 1.4: Hydrate-liquid-vapor equilibrium for the system methane+carbon dioxide+water. Each marker represents a different study of CH_4:CO_2 mixture equilibrium. Dotted lines connect data from a single reference, but do not imply modeling regression. (Herri *et al.*, 2011; Belandria *et al.*, 2011; Beltran & Servio, 2008)

1.3 Kinetics

Crystal growth can be divided in three phases according to Sunagawa (2005):

- A driving forces is applied on the system. This could be through supersaturation, supercooling or overpressure.
- A new phase composed of clusters, start forming. Some of these clusters form and dissociate, due to their small size. A particle reaches the critical size and nucleation of the crystal occurs.
- Once the crystal nucleates, it grows larger. This is known as the growth stage.

Supersaturation is defined as the difference in concentration at the saturation (equilibrium) temperature and concentration at the growth temperature (bulk) (Sunagawa, 2005). Supercooling (also known as subcooling in hydrate studies) is defined as a difference between growth temperature and equilibrium temperature (Sunagawa, 2005). Overpressure is the between the equilibrium vapor pressure and growth pressure (Sunagawa, 2005).

As hydrates are crystalline structures, they undergo the same process when forming. Several factors are known to affect hydrate nucleation and growth: subcooling, experimental conditions, composition and memory effect (Englezos, 1993a).

Several studies haven shown that nucleation time for hydrates is shortened after cycles of formation and dissociation. This creates "memory" in the water which allows for faster hydrate nucleation. Different hypotheses have been proposed to explain the memory effect with no conclusive evidence. Some of these include persistent crystallites or residual structures in water after dissociation (Sloan & Koh, 2008).

1.3.1 Nucleation

Figure 1.5 shows the mole consumption of a stirred-batch reactor kept at constant pressure and temperature against time. Initially moles are consumed until the guest reaches its equilibrium composition (Figure 1.5a-b). Moles of the guest dissolve until reaching supersaturation of the solution (Figure 1.5b-c). Once supersaturation is reached, mole consumption stops until nucleation occurs. The amount of time reported from supersaturation until nucleations starts is called induction time (Figure 1.5c-d). Moles are consumed and water becomes cloudy, indicating hydrate formation. This is when the growth phase starts, with constant consumption of the guest until reaching mass-transfer limitations. (Figure 1.5e-f) This hydrate formation resembles the general crystal growth process described on the previous section.

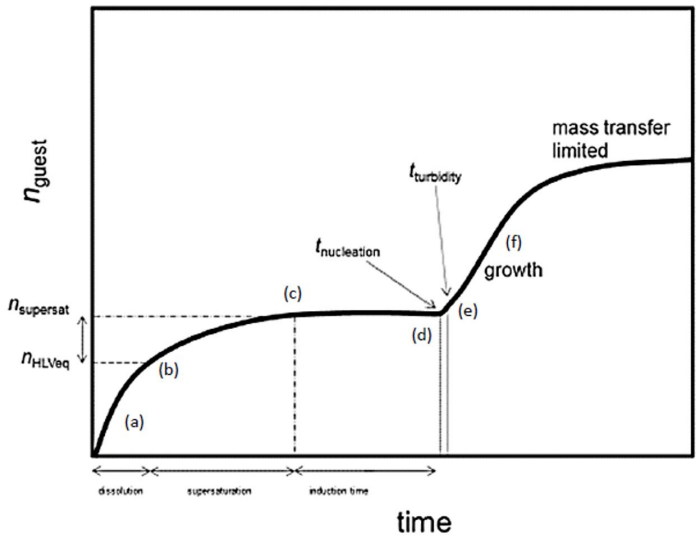

Figure 1.5: Moles of guest consumed vs time in a continuously stirred tank reactor at constant pressure and temperature. (a) Initial dissolution of the guest substance into the liquid phase. (b-c) Further guest dissolution achieves supersaturation. (c-d) This is the induction time, from the moment the solution is supersaturated until nucleation starts. (e) Liquid phase becomes opaque, the time from nucleation to turbidity is called turbidity time ($t_{\mathrm{turbidity}}$). (e-f) Hydrate growth phase starts until mass-transfer limitations are reached. Beltran (2021), personal communication.

1.3.2 Crystal Growth

Crystal growth or dissolution only occurs at the interface between the crystal and the bulk (Sunagawa, 2005). Two types of atomic interfaces exist: smooth and rough. Smooth atomic surfaces are flat while rough surfaces are comprised of kinks. Kinks are defined as a site where a step is bent Sunagawa (2005). Different growth mechanisms are observed for the smooth and rough atomic interfaces (Figure 1.6). The three growth mechanisms separated by $\Delta\mu/kT^*$ and $\Delta\mu/kT^{**}$. Driving force can be expressed as $\Delta\mu/kT^*$ where k is the Boltzmann constant, $\Delta\mu$ is the difference in chemical potential between two phases and T is temperature. At low driving forces ($< \Delta\mu/kT^*$), the atomic interface is smooth and a spiral growth mechanism controls crystallization. Between $\Delta\mu/kT^*$ and $\Delta\mu/kT^{**}$ the atomic surface is still smooth but a two-dimensional growth mechanism is observed. Once the driving force exceeds $\Delta\mu/kT^{**}$, the atomic surface becomes rough and an adhesive growth mechanism is expected (Sunagawa, 2005).

The location of the change in atomic interphase changes depending on the phase in which crystallization occurs (Sunagawa, 2005). Figure 1.7 shows the location of $\Delta\mu/kT^*$ and $\Delta\mu/kT^{**}$ for vapor phase (Figure 1.7a), solution phase (Figure 1.7b) and melt phase (Figure 1.7c) Sunagawa (2005). Hydrate formation occurs from a solution phase thus, changes in growth mechanism are expected to occur at relatively low

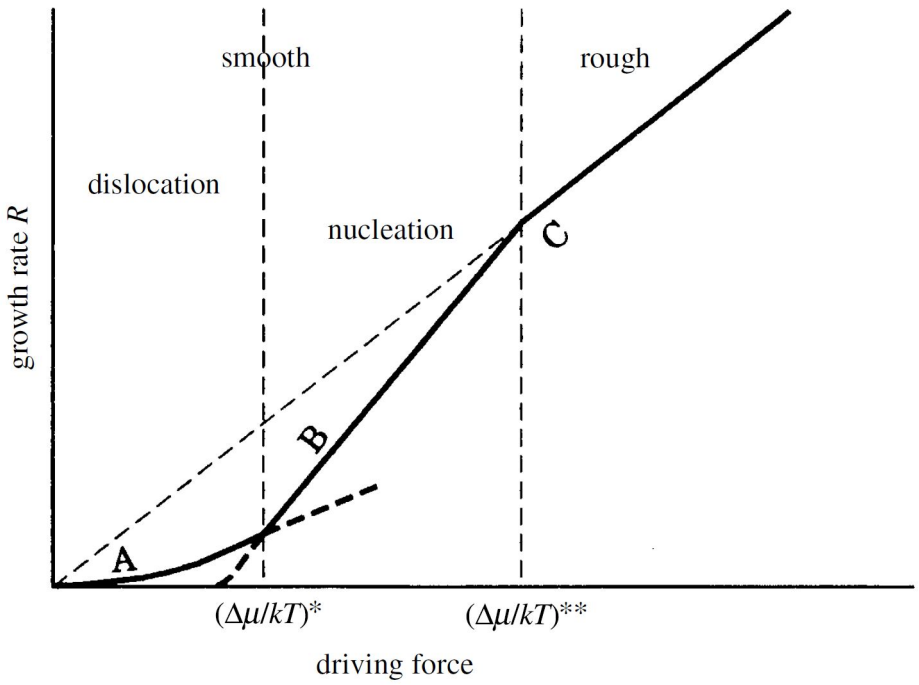

Figure 1.6: Driving forces where smooth or rough atomic interfaces are expected. $\Delta\mu/kT^*$ and $\Delta\mu/kT^{**}$ mark the change in growth mechanism. Curve A show a spiral growth mechanism. Curve B shows two dimensional growth. Curve C shows an adhesive type mechanism. Reproduced from Sunagawa (2005) (with permission).

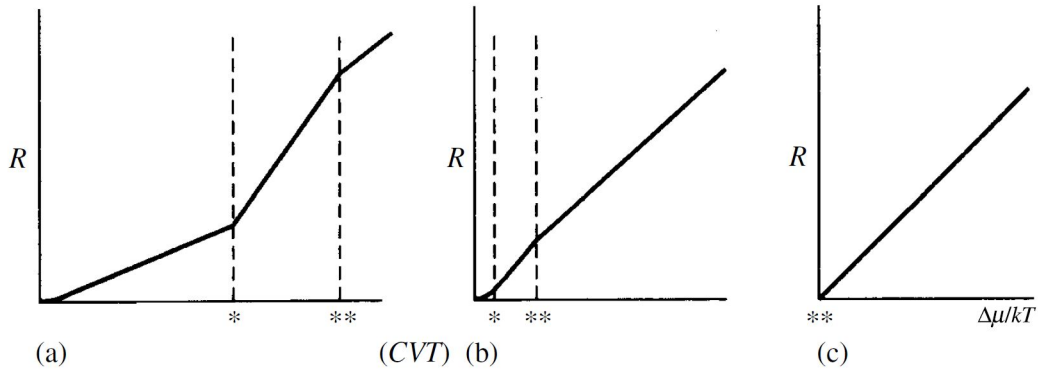

Figure 1.7: Position of $\Delta\mu/kT^*$ and $\Delta\mu/kT^{**}$ for different ambient phases. (a) Vapor phase. (b) Solution phase. (c) Melt phase. Reproduced from Sunagawa (2005) (with permission).

driving forces and in quick succession.

1.3.2.1 Gas Hydrate Growth

Pressure vessels used to study hydrate growth are usually equipped with windows, this allows for growth kinetics to be recorded in real time for quiescent systems.(Duquesnay *et al.*, 2016; Beltran & Servio, 2010; Peng *et al.*, 2007; Freer *et al.*, 2001) Generally, growth rates are calculated as the difference in size of the hydrate front after a set interval of time:

$$v_h = \frac{\Delta r}{\Delta t} = \frac{r_1 - r_0}{t_1 - t_0} \tag{1.2}$$

Where v_h is growth rate of the hydrate, r_1 and r_0 represent the position of the hydrate film interphase at times t_1 and t_0. An schematic of hydrate growth rate is seen on Figure 1.8. Images are acquired at t_0 and t_1 and difference in crystal size is recorded.

Hydrate growth rates have been studied using this time-dependent growth. Generally, subcooling has been used as an indicator of driving force for hydrate film growth, but overpressure can also been used (Beltran & Servio, 2010; Servio & Englezos, 2003). Daniel-David *et al.* (2015) studied the growth rates of CH_4, CO_2 and three CH_4+CO_2 mixtures. Generally, CO_2 was reported to have higher growth rates than CH_4 (Daniel-David *et al.*, 2015). Likewise, mixtures with higher content of CO_2 also reported higher growth rates than hydrates formed from a methane-rich feed (Figure 1.9).

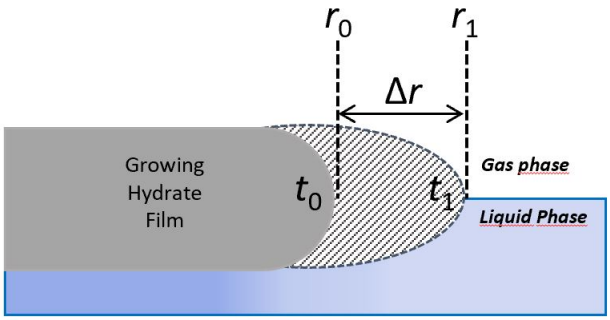

Figure 1.8: Schematic of growing hydrate film. Gray hydrate film is measured at t_0. In the time interval from t_0 to t_1, hydrate grows. The distance the hydrate grew in this interval is found by the difference between r_1 - r_0.

1.3.2.2 Analytical Techniques

Gas hydrates have been studied using different analytical techniques. Ripmeester *et al.* (1987) discovered structure H (Figure 1.1) using nuclear magnetic resonance (NMR) and X-ray powder diffraction. Gas chromatography is used to measure vapor-phase compositions during hydrate formation Sloan & Koh (2008); Uchida *et al.* (2005); Horvat *et al.* (2012). Raman spectroscopy was used to study the occupancy of cages within the crystalline hydrate structure (Uchida *et al.*, 2005; Schicks & Luzi-Helbing, 2013). Schicks & Luzi-Helbing (2013) used time-resolved Raman spectroscopy to observe the formation of individual cages of structures I and II during hydrate formation. The enclathration of CH_4 and CO_2 into structure I cages was monitored in real-time using this technique (Figure 1.10).

1.3.2.3 Driving Force

Crystals form when a deviation from equilibrium conditions exist, this is defined as driving force. Sunagawa (2005) describes a generalized driving force for crystallization as the difference in chemical potential between two phases. The difference in chemical potential can be related to deviations from equilibrium conditions in terms of temperature or of concentration. Even though both mechanisms are coupled during crystal growth, their contribution to crystal growth is not necessarily equal. For example, in a diluted ambient phase, condensation is required, making mass-transfer of higher importance. When studying condensed phases, such as melts, heat transfer plays an important role (Sunagawa, 2005).

For isobaric experimental setups, subcooling and mass-transfer driving forces can be used for hydrate growth. The degree of subcooling has been used extensively to represent driving force Beltran & Servio

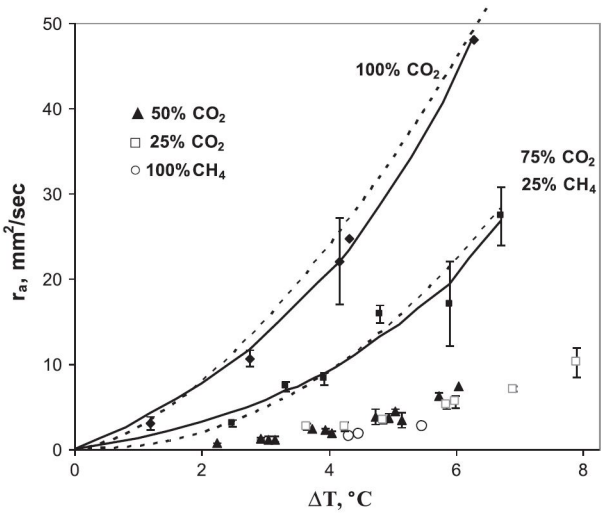

Figure 1.9: Growth rate in mm/sec vs subcooling/°C. Growth rates for CH_4, CO_2 and 3 CH_4:CO_2 mixtures (75:25, 50:50 and 25:75) are shown. Hydrate formed from CO_2-rich feed gas were reported to have higher growth rates than CH_4 rich hydrates at the same subcooling . Reproduced from Daniel-David *et al.* (2015) (with permission).

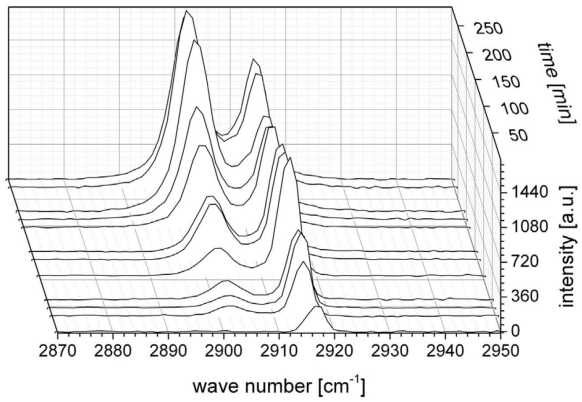

Figure 1.10: Real time Raman spectra of CH_4 forming 5^{12} and $5^{12}6^2$ cages. Reproduced from Schicks & Luzi-Helbing (2013) (with permission).

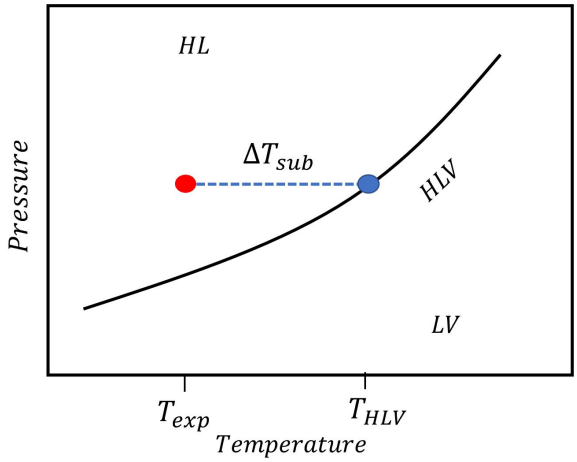

Figure 1.11: Schematic of a hydrate-liquid-vapor equilibrium curve. At constant pressure, ΔT_{sub} or the difference between experimental temperature (T_{exp}) and equilibrium temperature (T_{HLV}) can represent the driving force for hydrate growth.

(2010); Peng *et al.* (2007); Duquesnay *et al.* (2016); Tanaka *et al.* (2009b); Ueno *et al.* (2015); Li *et al.* (2013). Subcooling is defined as:

$$\Delta T_{sub} = T_{\mathrm{HLV}} - T_{\mathrm{exp}} \tag{1.3}$$

Where T_{HLV} is the hydrate-liquid-vapor equilibrium at experimental pressure, T_{exp} is the experimental temperature and ΔT_{sub} is the degree of subcooling. An schematic of the degree of subcooling can be observed on Figure 1.11. The magnitude of the difference between the HLV equilibrium temperature and the experimental temperature is representative of the driving force for hydrate growth of the system Vysniauskas & Bishnoi (1983).

The degree of subcooling is also associated with a difference in concentration at the interphase of a growing hydrate film. At constant pressure, T_{HLV} and T_{exp} have an corresponding equilibrium concentration. The difference in solubility between the growing hydrate interphase and the bulk liquid has been proposed as a representative mass-transfer limited driving force for hydrate growth (Saito *et al.*, 2010).

$$\Delta x_g = x_{eq,LV} - x_{eq,HLV} \tag{1.4}$$

Where $x_{eq,LV}$ is the liquid-vapor concentration of the guest at the experimental temperature, $x_{eq,HLV}$ is the concentration of the guest at hydrate-liquid-vapor temperature. Similar to ΔT_{sub}, the magnitude of

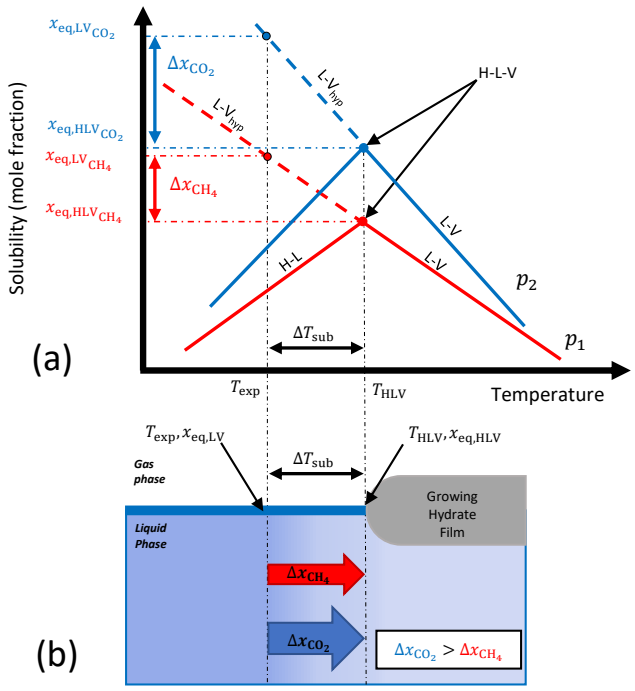

Figure 1.12: Solubility of guest molecules in the liquid phase. (a) Guest mole fraction in the liquid phase as a function of temperature. HLV, Hydrate-Liquid-Vapor equilibria; LV, Liquid-Vapor equilibria; LV_{hyp}, hypothetical Liquid-Vapor equilibria; HL, Hydrate-Liquid equilibria; Blue, CO_2; Red, CH_4. $p_1 > p_2$. (b) Schematic of the growing hydrate film occurring at constant pressure. The temperature and concentration at the HLV interface are assumed to be at the 3-phase equilibrium values (T_{HLV}, $x_{eq,HLV}$). The concentration at the L-V interface is assumed to be at the hypothetical 2-phase equilibrium value ($x_{eq,LV,hyp}$) at the experimental temperature (T_{exp}). Ovalle (2021), personal communication.

the difference in solubility (Δx_g) is representative of the driving for isobaric hydrate growth (Figure 1.12). The dotted lines marked as hypothetical represent an "extension" of the equation of state past the hydrate-liquid-vapor equilibrium temperature. This extension is used to calculate the equilibrium concentration of guest in bulk liquid ($x_{eq,LV}$).

Figure 1.12 shows why a mass-transfer driving might be better suited to model hydrate growth. At the same ΔT_{sub}, CO_2 has a higher Δx_g than CH_4. This is because solubility of CO_2 in water is approximately 20 times higher than CH_4 (Hashemi *et al.*, 2006). The effect of the difference in solubility can be observed on growth rate data graphed against subcooling (Figure 1.9). Growth rates are noticeably higher for CO_2 than for CH_4 at the same subcooling.

Kishimoto et al. (2012) proposed a similar model where volumetric growth is proportional to the difference in guest solubility at the hydrate-liquid-vapor interphase and bulk liquid (Δx_g). The difference with this model is the inclusion of the hydration number (n), which corresponds to the moles of water per

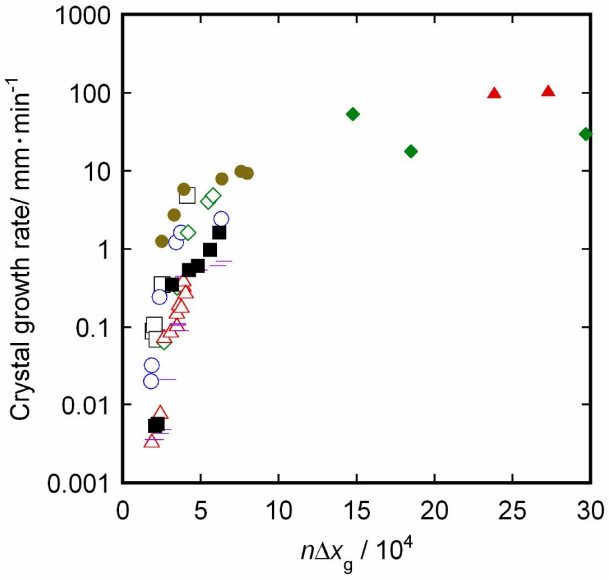

Figure 1.13: Growth rate in mm/sec vs nΔx_g. Growth rates for CH_4, CO_2 and 3 CH_4:CO_2 mixtures (75:25, 50:50 and 25:75) are shown. Hydrate formed from CO_2-rich feed gas were reported to have higher growth rates than CH_4 rich hydrates at the same subcooling. ◇ Methane. △, Propane. ▲, CO_2. ○, Methane. -, Propane. ■, Propane. Reproduced from Kishimoto & Ohmura (2012) (with permission).

mole of guest.

$$\dot{V}_h \propto n\Delta x_g \tag{1.5}$$

Kishimoto et al. (2012) showed growth rates correlate to nΔx_g of pure components. On Figure 1.13, Kishimoto & Ohmura (2012) graphed growth rates against nΔx_g for CH_4, CO_2 and C_3H_8 data. Growth rates seem to correlate better when compared to Figure 1.9. The correlation between nΔx_g and growth rates points to a mass-transfer limited driving force as ideal tool to study apparent kinetics of quiescent systems.

1.3.2.3.1 Dissociation during growth

Teng *et al.* (1996) hypothesized that growing hydrate crystals would reach a critical thickness during growth causing a collapse of the film. Moles of CO_2 are transferred both from the liquid phase towards the growing hydrate an vice-versa. Reformation would occur almost instantaneously given the available gas released by the hydrate. Ovalle & Beltran (2021) observed this phenomenon for propane and propane + methane hydrates. Using high resolution imaging, they showed portions of the growing hydrate film dissociating while the crystal growth front advanced on the water interface (Ovalle & Beltran, 2021).

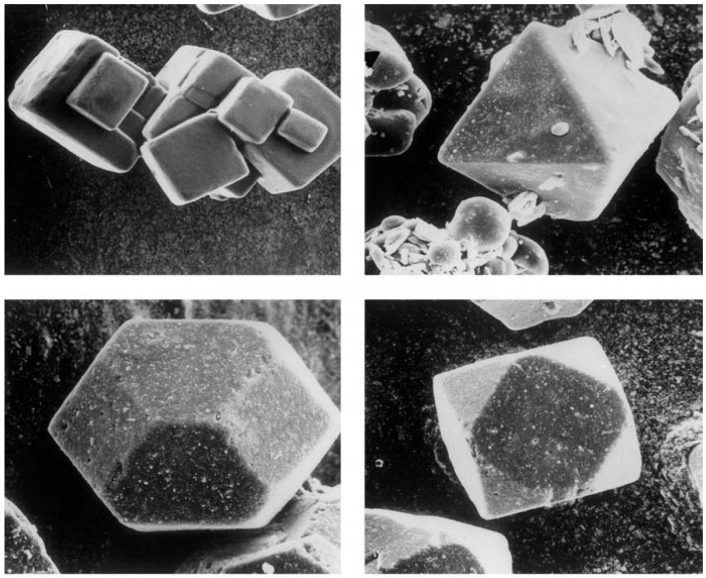

Figure 1.14: Morphology of sodium chloride crystal, same crystal structure but different crystal habit. Reproduced from Mullin (2001) (with permission).

1.3.3 Morphology

Morphology of a crystal is determined by internal and external factors. Crystal structure is the main internal factor while growth conditions and process are the external factors (Sunagawa, 2005). The same crystal structure can present different morphologies depending on the conditions of its growth. For instance, snow shows polyhedral forms as well as dendritic forms. These characteristic forms shown by crystals are also known as crystal habit (Mullin, 2001). An example can be observed on Figure 1.14, where sodium chloride formed four different crystal habits. Some of the conditions that have a considerable influence on crystal habit are supersaturation and subcooling (Mullin, 2001).

1.3.4 Morphology and Driving Force

Morphology and growth rate are both influenced by the process driving force (Sunagawa, 2005). As shown on Figure 1.15, these changes in growth mechanism are reflected in a sudden change of growth rate and morphology. (Sunagawa, 2005). At low driving forces ($< \Delta\mu/kT^*$), polyhedral morphologies are expected. As the driving force increases past $\Delta\mu/kT^*$, an abrupt change in morphology and growth rate is observed. In this range between $\Delta\mu/kT^*$ and $\Delta\mu/kT^{**}$, two-dimensional step-by-step growth is observed. At driving forces higher than $\Delta\mu/kT^{**}$, the atomic surface is rough allowing an adhesive growth mechanism resulting

in spherulitic or dendritic crystal habits.

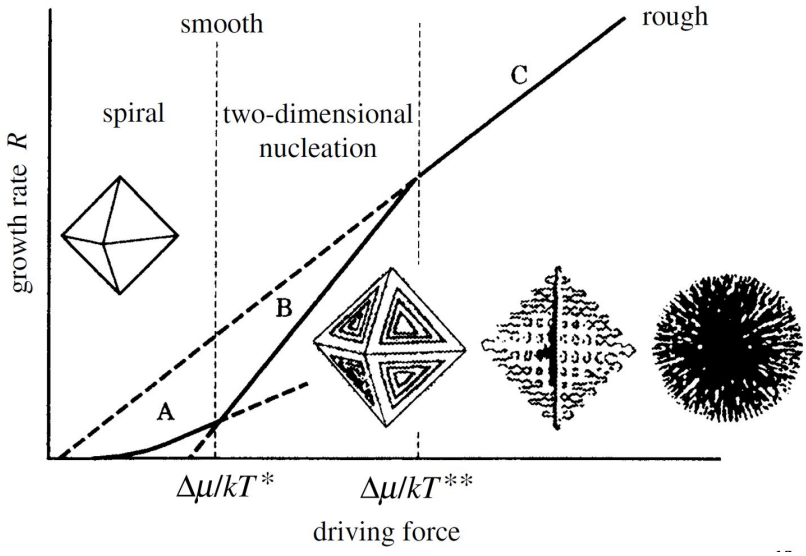

Figure 1.15: Growth rate as a function of driving force. $\Delta\mu$ is the difference in chemical potential between two phases, k is the Boltzmann constant and T is temperature. Morphology and growth rate show abrupt changes as driving force increases, specifically at $\Delta\mu/kT^*$ and $\Delta\mu/kT^{**}$. Reproduced from Sunagawa (2005) (with permission).

1.3.5 Morphology of Methane and Carbon Dioxide hydrates

Morphology of CO_2 and CH_4 hydrates have been extensively studied in the available literature.(Daniel-David *et al.*, 2015; Li *et al.*, 2014; Ohmura *et al.*, 2004, 2005; Servio & Englezos, 2003; Tanaka *et al.*, 2009a; Ueno *et al.*, 2015; Uchida *et al.*, 1999; Duquesnay *et al.*, 2016; Decarie & Beltran, 2011; Beltran & Servio, 2010) In general, it has been stated that morphology for these hydrate guests changes with increasing subcooling (Ohmura *et al.*, 2004). Servio & Englezos (2003) reported jagged and needle-like morphologies for both gases, as seen on Figure 1.16.

Carbon dioxide hydrates morphology has been reported to show several crystal habits (Figure 1.17). Peng reported rough, thick films. (Peng *et al.*, 2007) Ohmura *et al.* (2004) reported polyhedral, skeletal and dendritic hydrate films at low, medium and high subcoolings respectively. Uchida reported similar morphologies. (Uchida *et al.*, 1999) Other studies showed faceted, polyhedral and well defined crystal habits. (Daniel-David *et al.*, 2015; Ueno *et al.*, 2015)

Similarly, CH_4 hydrates have been reported to show several crystal morphologies (Figure 1.17). Multiple studies observed smooth and granular films. (Peng *et al.*, 2007; Daniel-David *et al.*, 2015; Duquesnay *et al.*,

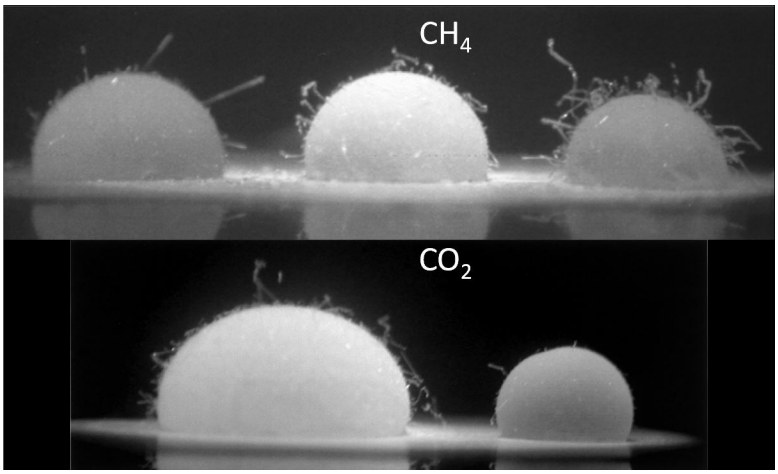

Figure 1.16: Morphology of CO_2 and CH_4 hydrates over a teflon stage. Jagged morphologies with needles are observed for both guests. Modified from Servio & Englezos (2003) (with permission).

2016) DuQuesnay observed a change in morphology from faceted to granular with increasing subcooling. Subramanian and Sloan observed a needle-like morphology for methane hydrates (Subramanian, 2002). Smelik & King (1997) reported polyhedral methane hydrates.

Mixed CH_4:CO_2 hydrate morphology have conflicting reports exist on literature. It is not clear whether the composition of feed gas has an effect on morphology. Daniel found that the composition of the mixed hydrate does have an effect on morphology (Daniel-David *et al.*, 2015). Conversely, Ueno et al. (2015) concluded that composition of the feed gas does not have an effect on morphology. Figure 1.18 shows the variability of morphologies observed in the literature.

Figure 1.19 shows some of the conditions used in literature. These studies have used differing ranges of conditions when studying morphology. From the experimental conditions shown on Figure 1.19 it is clear that the driving forces found in literature are different. Thus, it would be hard to draw conclusions only looking at literature data for morphology.

Experimental setups used to synthesize hydrates have also varied significantly, Figure 1.20 shows a few examples. Uchida et al.(1999) formed hydrates using liquid CO_2 in contact with water. Teflon stages with water droplets in contact with gaseous CO_2 and CH_4 have been used by different studies. (Servio & Englezos, 2003; Ueno *et al.*, 2015) Peng et al. (2007) formed hydrates using gaseous bubbles inside a mass of water.

Overall, a clear answer to the question *"Can methane and carbon dioxide hydrates look the same?"* has not been published in literature. The aim of this study is to give a clear answer to this question.

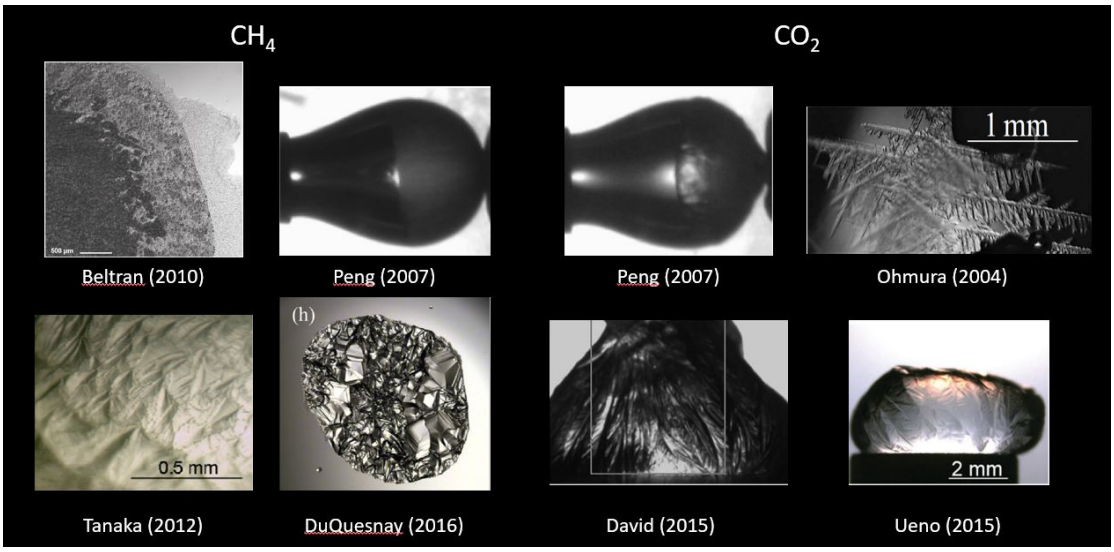

Figure 1.17: Morphology of CO_2 and CH_4 hydrates. The four left-most panels show morphology of CH_4 hydrates while right panel show CO_2 hydrates. Modified from Peng *et al.* (2007); Duquesnay *et al.* (2016); Beltran & Servio (2010); Ohmura *et al.* (2004); Tanaka *et al.* (2009a); Daniel-David *et al.* (2015); Ueno *et al.* (2015) (with permission).

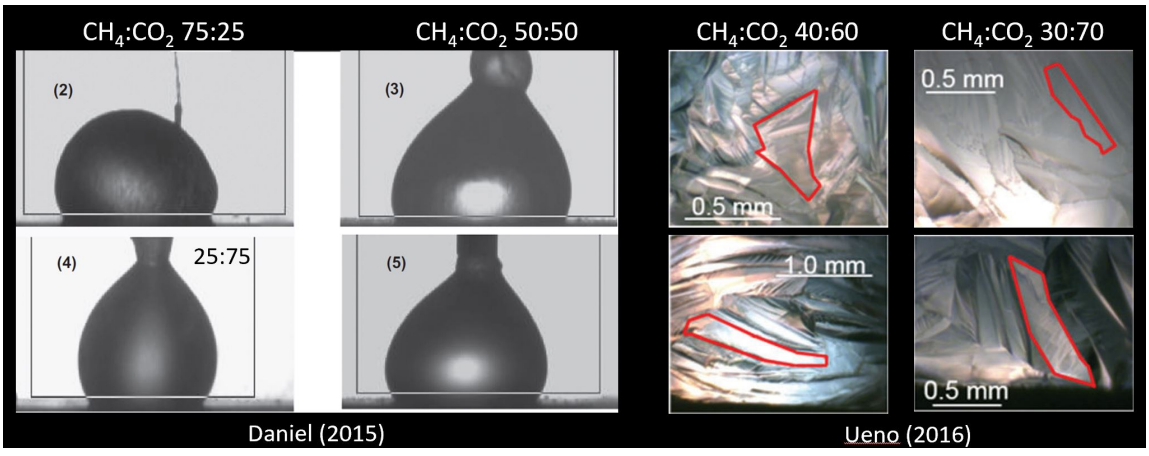

Figure 1.18: Morphology of CH_4:CO_2 hydrates. Composition of the specified above each pair of panels. Modified from Ueno *et al.* (2015); Daniel-David *et al.* (2015) (with permission).

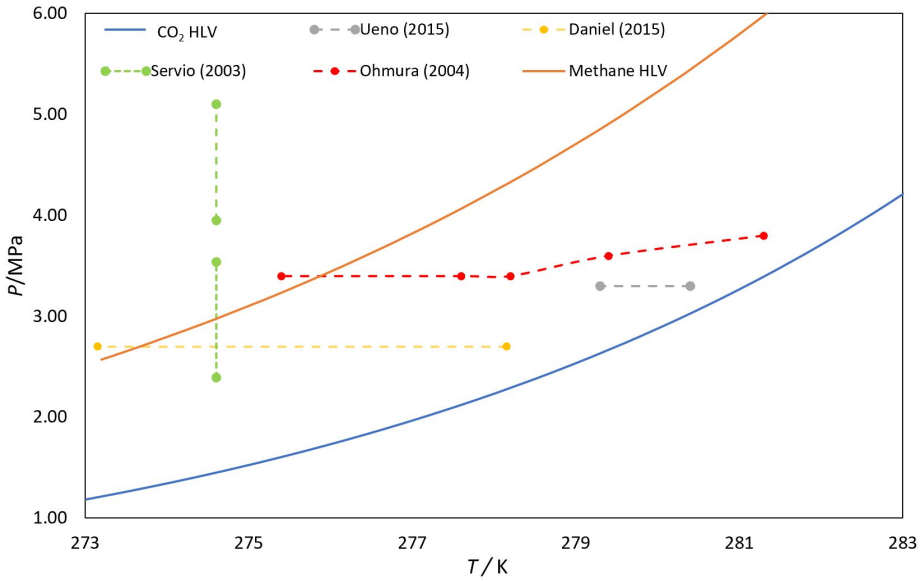

Figure 1.19: Partial phase diagram of methane and carbon dioxide. Points indicate experimental conditions used for different studies. Dotted lines are meant to indicate conditions used in the same study. (Servio & Englezos, 2003; Tanaka *et al.*, 2009a; Ueno *et al.*, 2015; Ohmura *et al.*, 2004)

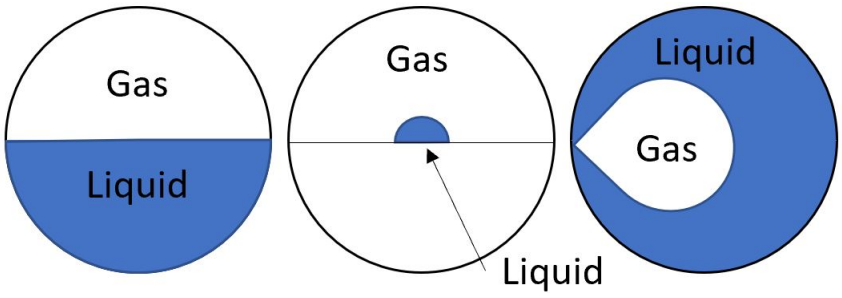

Figure 1.20: Schematic of experimental setups used in literature.

1.4 Previous work in the Beltran Lab

Pioneering work on methane and carbon dioxide hydrates was done by Decarie (2012) at the Royal Military College (Decarie & Beltran, 2011; Decarie, 2012). It was found that CH_4 and CO_2 formed different morphologies. However, control on experimental conditions was not ideal and warranted further investigation. Later Duquesnay *et al.* (2016) designed a new reactor that allowed tight control of experimental conditions. Experiments with this new 3-in-1 vessel allowed for better control of temperature and pressure and high-resolution imaging of hydrate growth. This technique is called 3-in-1 because morphology, growth rates and phase equilibria can be studied during a single experiment.

1.4.1 Methane & Carbon Dioxide

Using the 3-in-1 technique, Sandoval (2015) studied growth velocities, morphology and growth mechanism of methane and carbon dioxide. For these studies, subcooling and HLV equilibrium temperatures were matched, as seen on Figure 1.21. By matching T_{HLV} and ΔT_{sub}, the results would have comparable heat-transfer conditions.

Morphology of CH_4 and CO_2 was studied using a ΔT_{sub} of 2 and 3 K, as seen in Figure 1.22. Methane presented granular morphologies with smaller crystals as ΔT_{sub} increased. Carbon dioxide presented needle-like spherulites at both driving forces studied (Sandoval, 2015).

On Figure 1.23 experiments using a constant temperature gradient can be observed. Little to no effect of the temperature gradient was observed for CO_2. The needle-like morphology presented on uniform-temperature experiments persisted, getting smaller and more tightly packed with increasing temperature. A transition from faceted to granular crystal habit was observed for CH_4 hydrates at approximately ΔT_{sub} = 1.3 K .

Figure 1.24 presents growth rate data of CH_4 and CO_2 compared to ΔT_{sub}. At any given subcooling, CO_2 growth rates were an order of magnitude higher than those of CH_4 (Sandoval, 2015). Given that T_{HLV} was matched, it is clear that the solubility difference between both species had an important effect on growth rates.

Using Kishimoto & Ohmura (2012)'s driving force ($n\Delta x_g$), growth rates were graphed including data from literature. As seen in Figure 1.25, growth rate data seems to correlate to $n\Delta x_g$. It can also be seen in Figure 1.25 that the conditions used by Sandoval (2015) were such that $n\Delta x_g$ were an order of magnitude

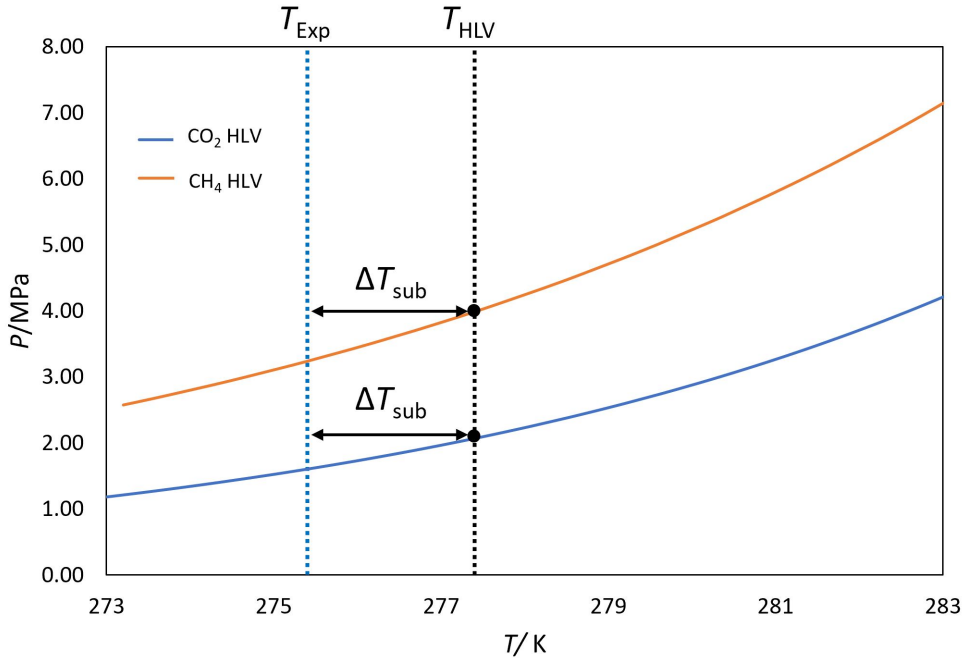

Figure 1.21: Schematic of experimental conditions used. Hydrate-liquid-vapor equilibrium temperatures were matched by using different experimental pressures. Orange line represents literature data for CH_4 HLV equilibrium. Blue line represents literature data for CO_2.

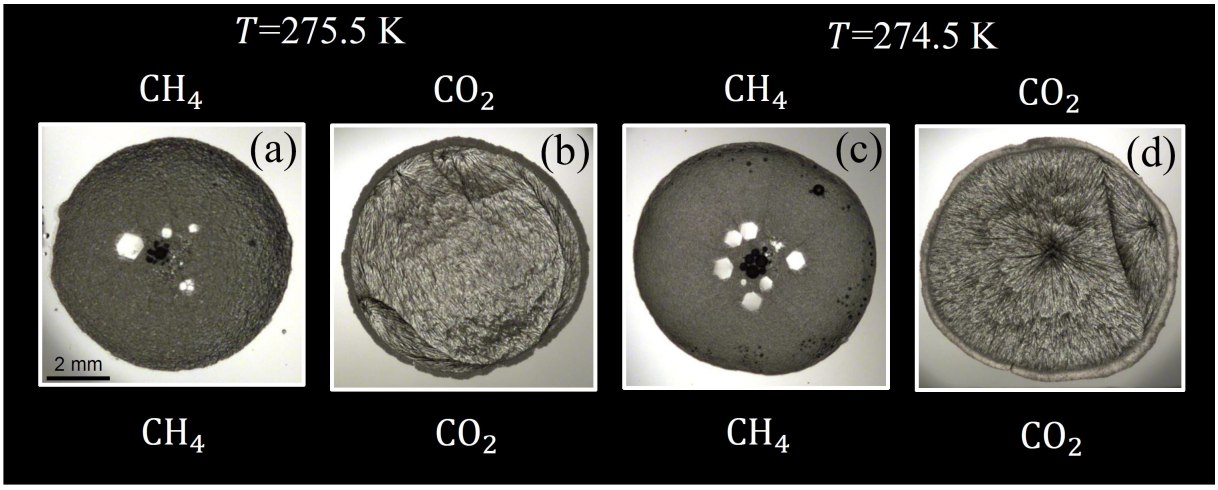

Figure 1.22: Hydrates formed with a uniform temperature setting. (a-b) T = 275.5 K. ΔT_{sub} = 2 K. (c-d) T = 274.5 K. ΔT_{sub} = 3 K. (a) CH_4 hydrate. P = 3.99 MPa. T_{HLV} = 277.39 K. (c) CH_4 hydrate. P = 4.00 MPa. T_{HLV} = 277.35 K. (d) CO_2 hydrate. P = 2.09 MPa. T_{HLV} = 277.45 K. Reproduced from Sandoval (2015).

different for methane and carbon dioxide.

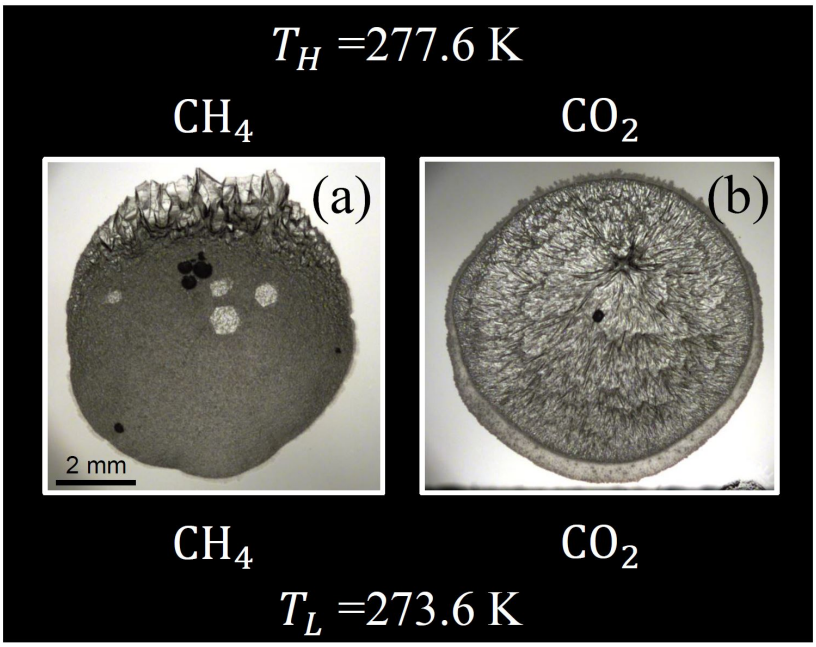

Figure 1.23: Methane and carbon dioxide hydrates formed using a constant temperature gradient. T_H and T_C correspond to hot and cold end temperatures set on the stage. CH_4, P = 3.98 MPa. T_{HLV} = 277.38 K. CO_2, P = 2.11 MPa. T_{HLV} = 277.54 K. Reproduced from Sandoval (2015).

1.4.2 Methane-Carbon dioxide mixtures

Following the work on pure CH_4 and CO_2 feed gases, CH_4+CO_2 mixtures were studied. The feed gas were 80:20 and 30:70 on a molar basis CH_4:CO_2. Experimental pressures were chosen to match HLV temperature along the different gases studied. Three different uniform temperature formation subcoolings were used, ΔT_{sub} of 1K, 2K or 4K. Constant temperature gradient formation and dissociation were used to evaluate morphology and phase equilibria.

Ortiz (2018) determined that at a same subcooling CH_4, CO_2, and CH_4:CO_2 hydrate morphologies are different. It was concluded that morphology of hydrates formed with CH_4, CO_2, and CH_4:CO_2 mixtures was found to be dependent on the CH_4:CO_2 ratio, as seen on Figure 1.26. As methane composition increased, crystal habit showed sensibility to ΔT_{sub}. Carbon dioxide hydrates showed a feather-like crystal habit at all subcoolings evaluated. The 30:70 mixture showed a radial crystal habit at all subcoolings, with crystallites getting closely packed as subcooling increased. The 80:20 mixture showed a noticeable transition. At low subcoolings crystal habit was quasi-faceted transitioning into granular to smooth at high subcoolings. CH_4 crystal morphology had a transition from faceted, polygonal crystals at low subcoolings to granular to spherulitic.

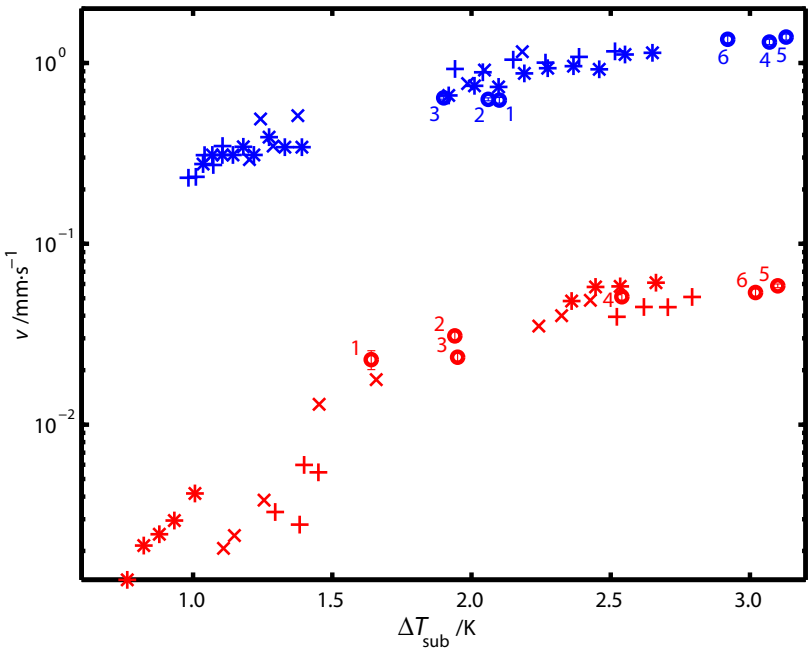

Figure 1.24: CO_2 (Blue markers) and CH_4 (Red markers) hydrate-film-growth velocity versus subcooling (ΔT_{sub}). ○ represent uniform surface experiments, and the other markers correspond to temperature gradient experiments. Error bars are equal to one standard deviation. +, P = 2.13 MPa. ✱, P = 2.10 MPa. ×, P = 2.08 MPa. ^{1}○, P = 2.09 MPa. ^{2}○, P = 2.09 MPa. ^{3}○, P = 2.08 MPa. ^{4}○, P = 2.08 MPa. ^{5}○, P = 2.12 MPa. ^{6}○, P = 2.08 MPa. +, P = 3.94 MPa. ✱, P = 4.00 MPa. ×, P = 4.01 MPa. ^{1}○, P = 3.97 MPa. ^{2}○, P = 4.01 MPa. ^{3}○, P = 4.00 MPa. ^{4}○, P = 3.99 MPa. ^{5}○, P = 4.01 MPa. ^{6}○, P = 4.00 MPa. Reproduced from Sandoval (2015).

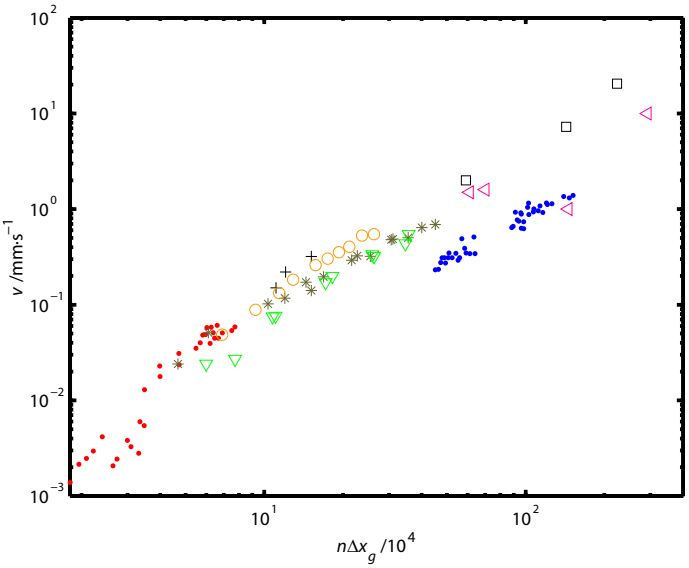

Figure 1.25: CO_2 and CH_4 hydrate-film-growth velocity versus the difference in solubility ($n\Delta x_g$). ●, CO_2 Sandoval (2015). ◁, CO_2 (Uchida *et al.*, 1999). ▫, CO_2 (Daniel-David *et al.*, 2015). ●, CH_4 This work. +, CH_4 (Daniel-David *et al.*, 2015). ○, CH_4 (Li *et al.*, 2014). ✱, CH_4 (Freer *et al.*, 2001). ▽ CH_4 (Kitamura & Mori, 2013). Reproduced from Sandoval (2015).

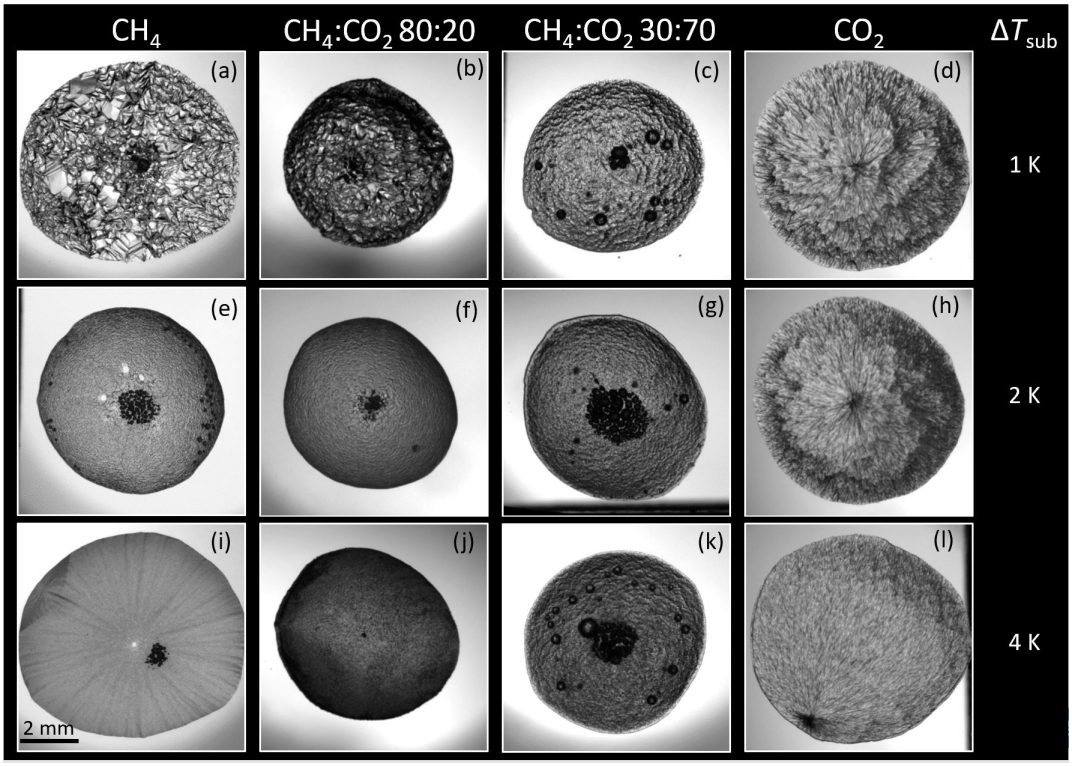

Figure 1.26: CH_4, CO_2, and CH_4:CO_2 hydrates formed using a uniform temperature setting. (a)-(d) T_{exp} = 276.5 K. (e)-(h) T_{exp} = 275.5 K. (i)-(l) T_{exp} = 273.5 K. (a), (e), (i) CH_4 hydrates, P = 4.03 MPa. (b), (f), (j) CH_4:CO_2 80:20 hydrates, P = 3.25 MPa. (c), (g), (k) CH_4:CO_2 70:30 hydrates, P = 2.35 MPa. (d), (h), (l) CO_2 hydrates, P = 2.10 MPa. Reproduced from Ortiz (2018).

Figure 1.27 shows measured growth rates at different ΔT_{sub} studied by Ortiz (2018). Similar to the Sandoval (2015), growth rates for CO_2 rich hydrates are considerably higher than that of CH_4-rich.

Sections 1.4.2 and 1.4.1 shows studies on the effect of subcooling on CH_4, CO_2, and their mixtures. Overall, using ΔT_{sub} as a driving force showed stark differences in growth rate and morphology between the CH_4 and CO_2. Both studies proposed this is evidence that hydrate growth is a mass-transfer limited process.

In summary, all the data from literature indicates that a mass-transfer limited driving force is well suited to study hydrate kinetics. No study in the available literature has attempted to unify morphology and growth rates using a mass-transfer driving force. Given all the evidence I hypothesize: a mass-transfer limited driving force as described by Kishimoto & Ohmura (2012) will accurately correlate to growth rates in quiescent systems and its effect on morphology.

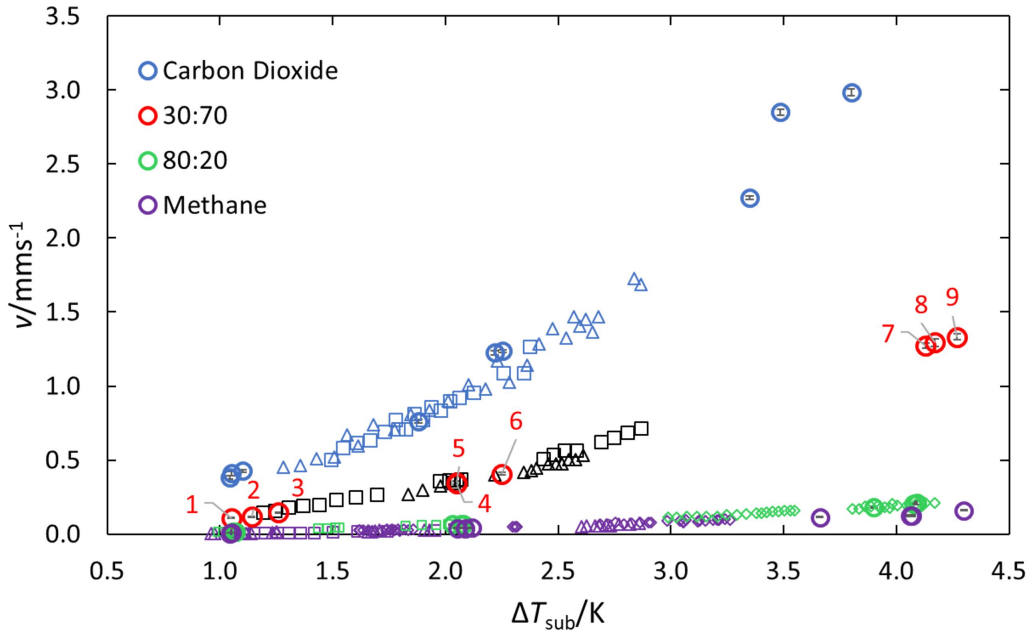

Figure 1.27: Growth rate vs ΔT_{sub} for CH_4, CH_4:CO_2 80:20, CH_4:CO_2 30:70 and CO_2 hydrates. Red markers indicate growth rate of 30:70 hydrates formed under uniform surface temperature profile. Black markers show the measured growth rate of 70:30 hydrates formed under constant temperature gradient profile. CH_4 (purple markers), 80:20 (green markers) and CO_2 (blue markers) hydrate growth rate is shown for comparison. △, P = 3.25 MPa. □, P = 3.25 MPa. ^{1}○, P = 2.35 MPa. ^{2}○, P = 2.35 MPa. ^{3}○, P = 2.35 MPa. ^{4}○, P = 2.35 MPa. ^{5}○, P = 2.36 MPa. ^{6}○, P = 2.35 MPa. Reproduced from Ortiz (2018).

1.5 Objectives

Overall, several studies on morphology of CH_4, CO_2, and CH_4:CO_2 mixed hydrates have been published. Some studies say CH_4 and CO_2 have similar morphologies while other state they look different. The effect of composition on CH_4:CO_2 hydrates also present conflicting reports. Reports in literature have used an array of different conditions and experimental setups to study morphology. Kishimoto & Ohmura (2012) used a mass-transfer model that seems to accurately correlate growth rates of different hydrate formers. Taking all of this into account the objectives of this study are:

- Use a mass-transfer limited driving force to evaluate kinetics and morphology of CH_4, CO_2, and CH_4:CO_2 hydrates.
- Prove that nΔx_g is an appropriate surrogate for the difference in chemical potential between phases.
- Find an answer to the question: "Do CH_4 and CO_2 hydrates look the same?" to resolve apparent contradictions in the available literature.

Chapter 2

Experimental

2.1 Apparatus

A 3-in-1 reactor developed by Duquesnay *et al.* (2016) was used during this study (Figure 2.1). It consists of a 316 stainless steel cell fitted with two sapphire windows (Rayotek, CA, USA) that allow for a bird's-eye view of the sample. Temperature inside the vessel was monitored using a Pt RTD probe (Omega Engineering, Canada). Pressure was measured with Rosemount 3051S pressure transmitter (Laurentide Controls, QC, Canada). The apparatus was illuminated with a Schott KL2500 LCD cold light source (Optikon, ON, Canada). Images were acquired using a PCO.edge 5.5 sCMOS camera equipped with a NIKON AF-Micro-Nikkor 60 mm lens (Optikon, ON, Canada). The reactor was cooled using a Thermo Scientific AC 200 refrigerated circulator (Fischer Scientific, Canada) connected to a copper coil wrapped around the reactor.

2.1.1 Stage

Stage temperature was controlled with a High Pressure Bilateral Control Stage (HP-BTCS), shown on Figure 2.2. Thermoelectric cooler modules (TEMs) were placed on each end of the stage (TE Technology, MI, USA) with copper plates attached to ensure effective thermal conductivity. TEM temperature was measured by a thermistor placed on each end of the stage. (TE Technology, MI, USA). Bi-polar PID temperature controllers (TE Technology, MI, USA) control temperature of the TEMs. This setup allows for two formation settings. Uniform formation setting consists of equal temperatures for both ends of the stage (Figure 2.3a). Gradient formation allows for different temperatures at each end of the stage (Figure 2.3b). The difference

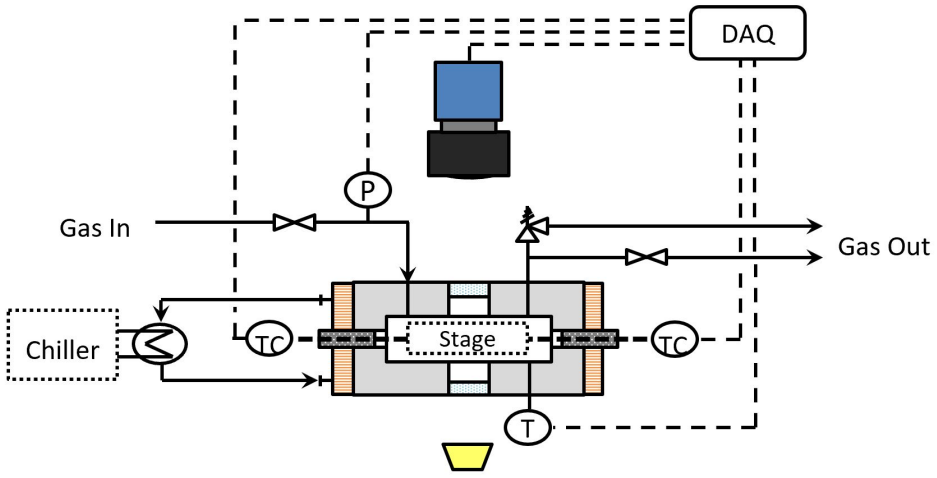

Figure 2.1: Schematic of the apparatus used for experimentation. Duquesnay *et al.* (2016)

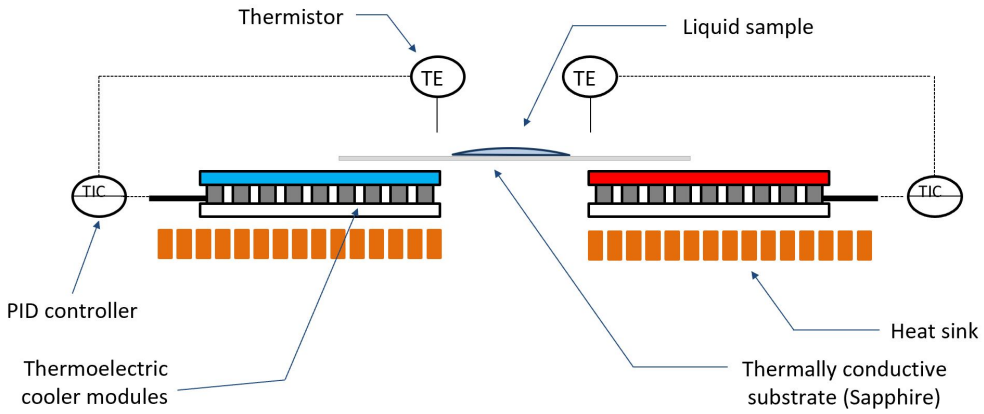

Figure 2.2: Schematic of the High Pressure Bilateral Control Stage.Duquesnay *et al.* (2016)

in temperature across the stage allows for multiple subcoolings to be studied simultaneously (Figure 2.3).

2.1.2 Materials

Table 2.1 shows the gases used to form hydrates in this study. All these gases were sourced from Air Liquide (QC, CA). Distilled and deionized water was obtained in-house. 99.99% nitrogen (Air Liquide, QC, CA) was also used.

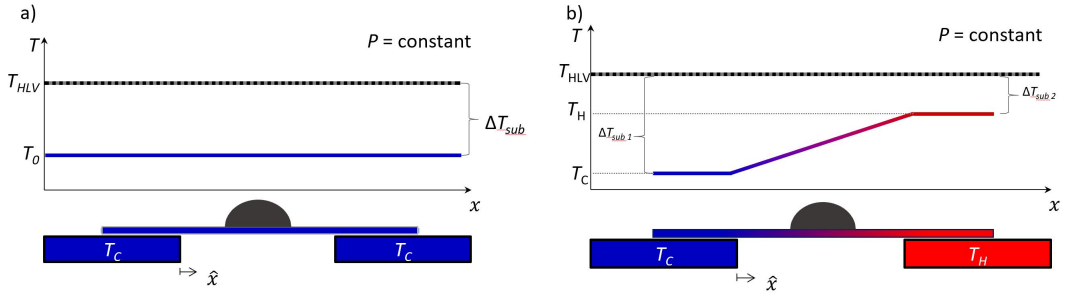

Figure 2.3: Hydrate formation settings. a) Uniform temperature formation. Both thermoelectric modules are set to the same temperature, one subcooling is set across the stage. b) Constant temperature gradient formation. Different temperatures are set for each thermoelectric module. Multiple subcoolings are evaluated across the stage.

Table 2.1: Gases used in this study. Nominal compositions (CH_4:CO_2) are as follows: Mixture 1 (80:20); Mixture 2 (30:70).

Composition	$10^2 y_{CH_4}$	$10^2\ y_{CO_2}$	Source
CH_4	99.999	0	
80:20	80.02	19.98	Air Liquide,
30:70	29.94	70.06	QC, CA
CO_2	0	100	

2.2 Methods

Sapphire slides (Rayotek, CA, USA) were cleaned with liquid detergent and rinsed with deionized water. Clean sapphire slides were then submerged in acetone and subsequently in isopropanol for 5 minutes each in a sonicator bath. Before placing the sapphire slide on the stage, a small amount of thermal paste was applied on the copper plates. This is meant to ensure even heat transfer across the slide. Once the sapphire slide was set over the copper plates, a 20 μL deionized water droplet was placed on the slide using a micropipette. The reactor was then sealed and wrapped with the copper coil. The sealed vessel was purged 3 times with 99.99% nitrogen (Air Liquide, QC, CA) and 3 times with one of the experimental gases (Table 2.1).

2.2.1 Pretreatment of samples

Once the pressure vessel was sealed and purged, temperature of the vessel was decreased at atmospheric pressure until ice was formed (Figure 2.4a-b). Once ice was formed, pressure inside the vessel was increased to experimental conditions (Figure 2.4b-c). Ice was thawed by increasing the temperature above the ice point, forming hydrates (Figure 2.4c-d). The hydrates formed from ice are then dissociated by increasing the temperature from the hydrate-liquid to liquid-vapor region (Figure 2.4d-e). This pretreatment is done to

ensure memory effect in the droplet (Section 1.3).

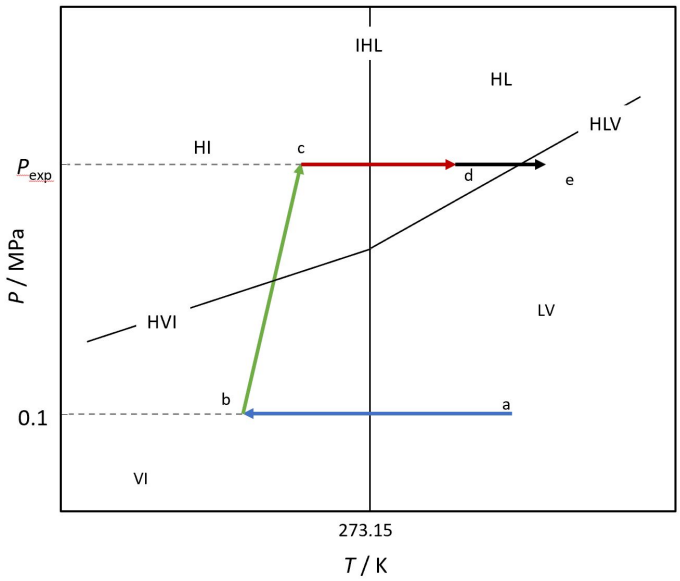

Figure 2.4: Pretreatment of the droplet done to ensure memory effect during the experiment. a-b) Droplet is frozen by decreasing the temperature inside the vessel at atmospheric pressure. b-c) Once ice has formed, the pressure of the vessel is increased to P_{exp}. c-d) Ice is melted, forming hydrates. d-e) Hydrates from ice are dissociated by increasing stage temperature. I, ice. H, hydrate. V, vapor. L, liquid.

2.2.2 Hydrate formation

After dissociating hydrates from ice, the droplet was kept 1 K above HLV temperature until no crystallites were observed. Two hydrate formation settings were used , uniform temperature (Figure 2.3a) and constant temperature gradient (Figure 2.3b). The temperature was decreased at a constant pressure under HLV conditions to set a subcooling. Within minutes, nucleation started and crystal growth was observed. During constant temperature gradient experiments, a difference of 4 K was set along the stage.

2.2.3 Experimental conditions

Table 2.2 shows all the experimental conditions used during this study.

Table 2.2: Experimental conditions for gas hydrate formation from water droplets immersed in guest atmosphere. T_{HLV}, measured H-L-V equilibrium temperature at experimental pressure. T_H, Highest temperature of the stage. T_L, Lowest temperature of the stage.

Expt	Feed gas	P /MPa	T_{HLV} /K	T_H /K	T_L /K
1	CH_4	4.00	277.4	279.2	275.2
2	CH_4	4.00	277.4	279.0	275.0
3	CH_4	4.01	277.5	279.0	275.0
4	CH_4	4.00	277.4	276.9	276.9
5	CH_4	4.00	277.4	277.1	277.1
6	CH_4	6.60	282.3	274.4	274.4
7	CH_4	8.60	284.7	275.5	275.5
8	CH_4	8.60	284.7	276.7	276.7
9	CO_2	2.10	277.5	277.5	277.5
10	CO_2	2.09	277.5	277.5	277.5
11	CO_2	2.09	277.5	277.5	277.5
12	CO_2	2.10	277.5	279.5	275.5
13	CO_2	2.10	277.5	279.0	275.0
14	CO_2	2.10	277.5	275.7	279.7
15	80:20	3.25	277.4	279.2	275.2
16	80:20	3.25	277.4	275.0	279.0
17	80:20	3.25	277.4	273.5	277.5
18	80:20	3.25	277.4	271.8	275.8
19	80:20	3.25	277.4	277.1	277.1
20	80:20	3.25	277.4	277.2	277.2
21	80:20	3.25	277.4	277.1	277.1
22	80:20	4.40	280.2	274.2	274.2
22	80:20	4.40	280.2	273.4	273.4
23	30:70	2.35	277.4	277.3	277.3
24	30:70	2.35	277.4	277.2	277.2
25	30:70	2.35	277.4	277.3	277.3
26	30:70	2.35	277.4	279.5	275.5
27	30:70	2.35	277.4	279.2	275.2
28	30:70	2.35	277.4	277.2	277.2
29	30:70	2.35	277.4	277.1	277.1
30	30:70	2.35	277.4	274.2	274.2
31	30:70	2.35	277.4	276.4	276.4
32	30:70	2.35	277.4	275.4	275.4
33	30:70	2.35	277.4	273.4	273.4

2.2.4 Mass transfer limited driving force

2.2.4.1 Pure components

The mass-transfer driving force proposed by Kishimoto & Ohmura (2012) was used in this study. The driving force in this model depends on the difference in solubility between the growing hydrate film and the bulk liquid. To find the molar composition of pure gases in the liquid phase Englezos *et al.* (1987a) proposed:

$$x_{eq,LV} = \frac{f(T,P)}{H} \tag{2.1}$$

Where $x_{eq,LV}$ is the mole fraction of the feed gas, f is the fugacity of the guest at experimental temperature and pressure and H is Henry's constant. Fugacity of the pure components was found using the Trebble-Bishnoi equation of state (Trebble & Bishnoi, 1987). Henry's constant for CH_4 and CO_2 were taken from Fogg & Gerrard (1991).

2.2.4.2 Extension to mixtures

In order to extend Kishimoto's treatment to mixtures, it is necessary to modify the equilibrium expression as follows:

$$x_{i,eq,LV} = y_i \frac{f_i(T,P)}{H_i} \tag{2.2}$$

Where ideal solution and infinite dilution in the liquid phase were assumed. In addition, it is necessary to account for the presence of two guests as follows:

$$\nu_1 g_1 + \nu_2 g_2 + n\mathrm{H_2O} \rightleftharpoons 1\mathrm{Hyd} \tag{2.3}$$

Where g are the hydrate guests, n is the hydration number and ν are the stoichiometric coefficients of each guest. This coefficient is found through the hydrate phase composition. The Herriot Watt University HWPVT software was used to establish the stoichiometric coefficients and hydration number for the two mixtures. Volumetric growth rate of the hydrate film is then expressed as:

$$\dot{v_h} = \frac{\dot{m}_g(\nu_1 M_{g_1} + \nu_2 M_{g_1} + nM_W)}{\rho_h} \tag{2.4}$$

In this case $\dot{m_g}$ is the molar flux of both guests into the hydrate phase. This equivalence can be expressed with the stoichiometric coefficient of one guest.

$$\dot{m_g} = \frac{\dot{m}_{g_1}}{\nu_1} \tag{2.5}$$

Where $\dot{m}_{g_1}$ is the molar flux of guest 1 at the surface of the growing hydrate, expressed as:

$$\dot{m}_{g_1} = h_{m,g_1}\rho_l \Delta x_{g_1} \tag{2.6}$$

Where h_{m,g_1} is the mass transfer coefficient for guest 1, ρ_l is the molar density of water and Δx_{g_1} is the difference in liquid mole fraction of guest 1 between HLV and experimental conditions. Density of the hydrate is defined by:

$$\rho_h = \frac{(N_w/n)(\nu_1 M_{G_1} + \nu_2 M_{G_1} + nM_W)}{Aa^3} \tag{2.7}$$

Where A is the Avogrado number, N_w is the number of water molecules in each unit cell and a is the lattice constant of the hydrate. Substituting $\dot{m}_{g_1}$ and ρ_h in the volumetric growth rate equation:

$$\dot{v_h} = h_{m,g_1}\left(\frac{a^3\rho_l A}{N_w}\right) n\frac{\Delta x_{g_1}}{\nu_1} \tag{2.8}$$

Kishimoto & Ohmura (2012) assumed $h_{m,g}$ is proportional to $D_{g,w}$, the diffusion coefficient of the guest in water and variations of $D_{g,w}$ are deemed insignificant compared to Δx_g. This results in the following correlation:

$$\dot{v_h} \propto \frac{n\Delta x_{g_1}}{\nu_1} \tag{2.9}$$

Chapter 3

Results and Discussion

3.1 Morphology

Figure 3.1 shows hydrates formed with a uniform temperature setting (Figure 2.3a). Experimental pressures were different for each gas mixture; this was necessary in order to match hydrate-liquid-vapor equilibrium temperature (T_{HLV} = 277.5 K). Experimental conditions for the presented images are specified at the bottom of Figure 3.1. Top panels present images of the early stages of hydrate growth, where crystals exhibited opaque, faceted, euhedral habits. A two-dimensional growth mechanism is observed for each guest. Evidence for two-dimensional growth is easily observable as striations on the newly formed crystals (Figure 3.1 top panels).

Using our extension of Kishimoto & Ohmura (2012)'s model (Section 2.2.4.2), the solubility of CH_4 or CO_2 was used to find a measure of driving force in terms of the difference in solubilities at HLV equilibrium and HL equilibrium (Figure 1.12). The $n\Delta x_g$ of the 80:20 and 30:70 mixtures on Figure 3.1 were calculated in terms of methane mole fractions. At low driving forces ($n\Delta x_g$ < 2.0), methane served to predict morphology qualitatively: similar driving forces resulted in comparable morphologies. In the case of carbon dioxide hydrates, CO_2 was used to calculate $n\Delta x_g$.

Bottom panels show water samples fully covered by hydrates. Except for pure carbon dioxide, the hydrate surface appears rugged. At first sight of the bottom panels in Figure 3.1, it might be tempting to say that morphologies are different. However, this apparent difference was due to partial dissociation of the growing crystals.

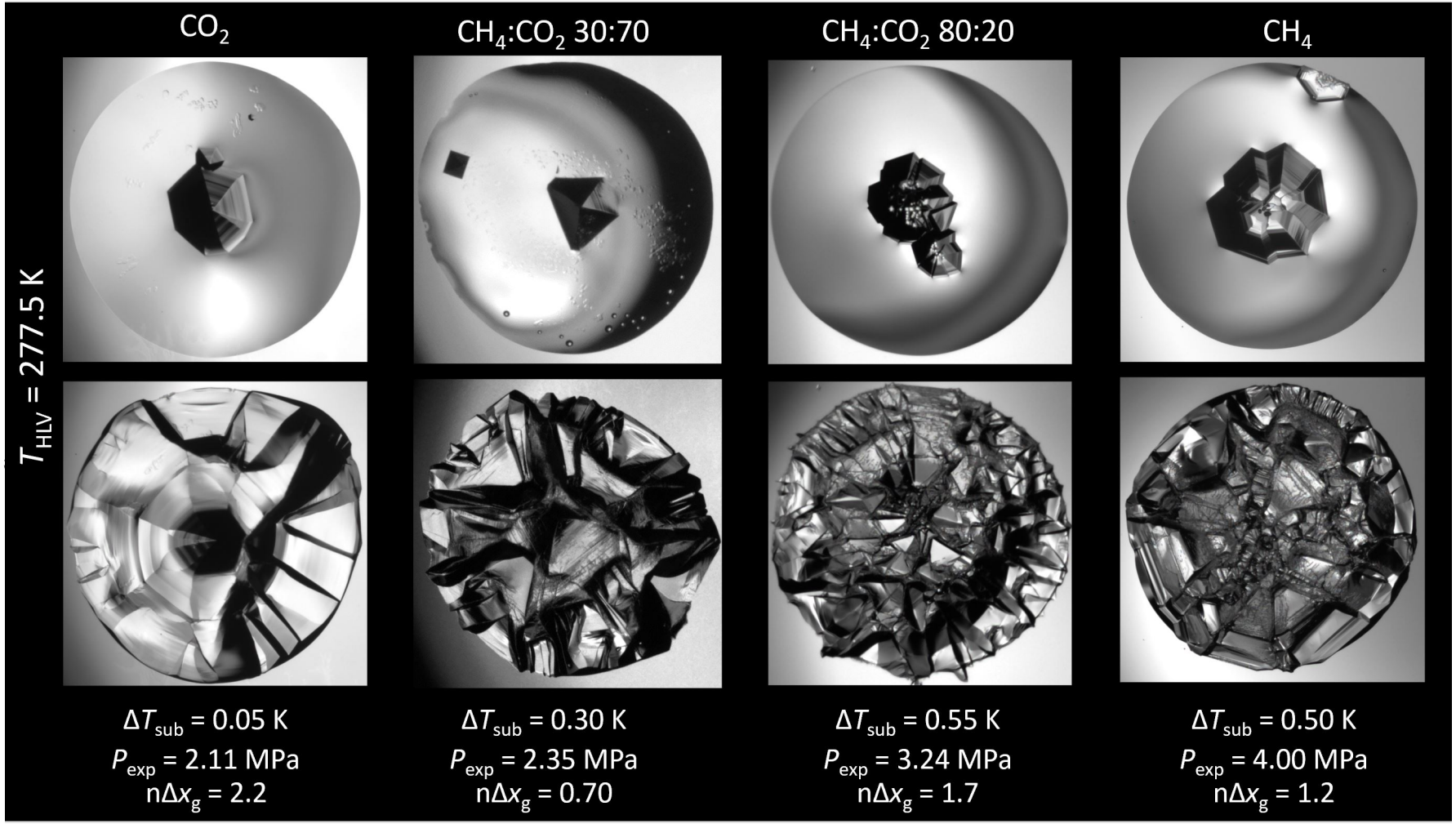

Figure 3.1: Gas hydrates formed at a uniform temperature setting. Feed gas composition is specified above each pair of pictures. Top panels show initial stages of hydrate film growth. Bottom panels show fully covered water droplets. Values of $n\Delta x_g$ of mixtures were calculated using the solubility of methane. T_{HLV} = 277.5 K for all experiments. Driving force in both ΔT_{sub} and $n\Delta x_g$ are shown.

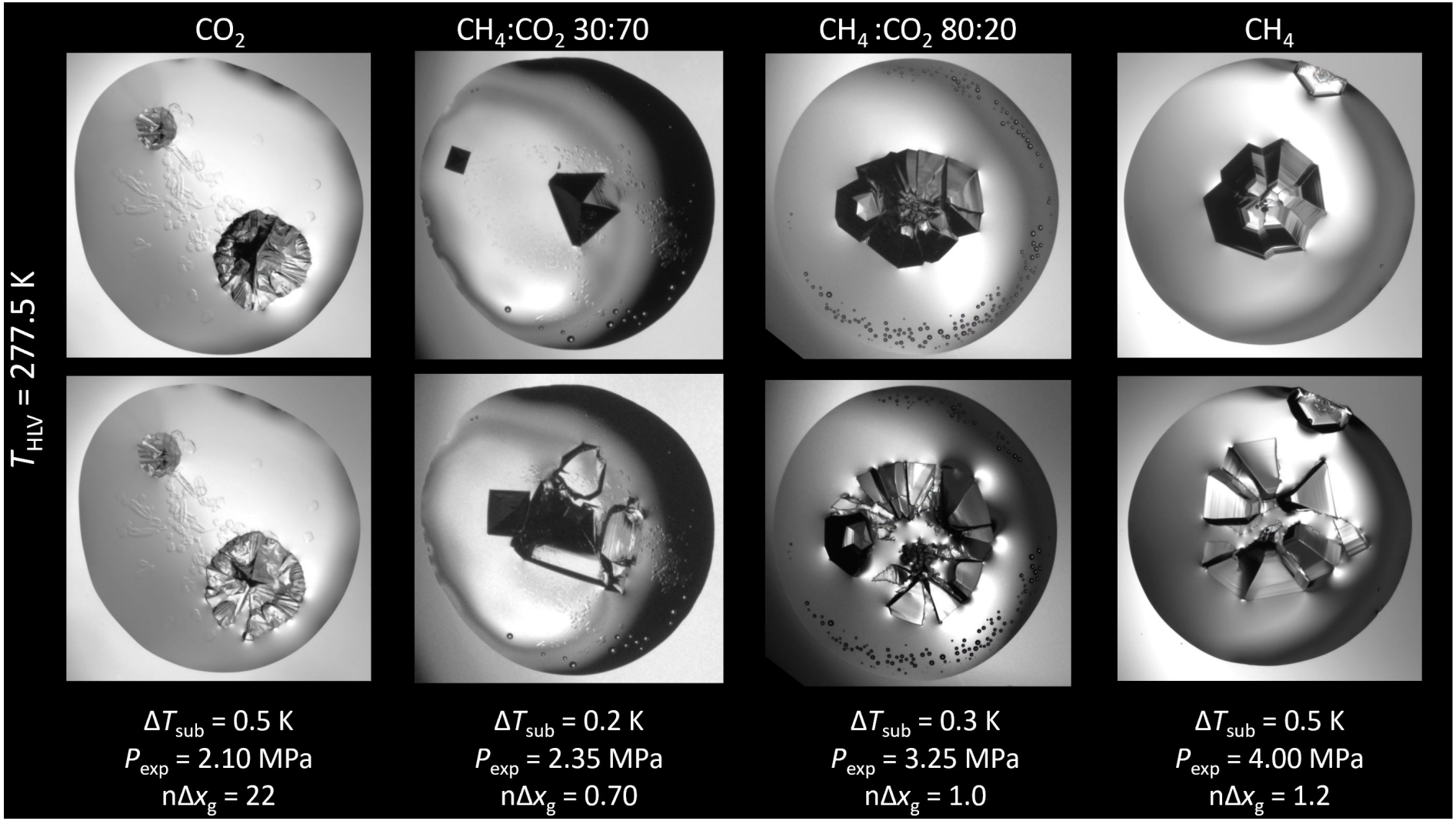

Figure 3.2: Partial dissociation of hydrates formed at a uniform temperature setting is shown. Feed gas composition is specified above each pair of pictures. Top panels show growth before partial dissociation was observed. Bottom panels present the change in morphology after partial dissociation. T_{HLV} = 277.4 K for all experiments. The driving force in both ΔT_{sub} and $n\Delta x_g$ are shown at the bottom of the figure.

Figure 3.2 shows instances of partial dissociation during growth. As the hydrate film grew, crystallites partially dissociated, leaving pieces of the previously formed hydrate, from which hydrate continued to grow. Before partial dissociation, hydrates appeared gray. However, ensuing growth produced a translucent film. The change in hue could indicate a change in the thickness of the film or in the angle at which light passes through the hydrate. Partial dissociation occurred regardless of temperature profile and at no particular time of growth or location. At all driving forces, all guests showed partial dissociation during growth. Partial dissociation was considerably less frequent during growth of CO_2 hydrates. Ovalle & Beltran (2021) first showed this partial dissociation mechanism for propane and methane + propane mixtures. To the best of my knowledge, this is the first time this partial dissociation is shown for methane, carbon dioxide and their mixtures.

Partial dissociation occurred regardless of temperature profile, location in the droplet or time of growth. At all driving forces, all guests showed partial dissociation during growth. However, partial dissociation was much more frequent with gases containing methane. The disparity in dissociation/growth frequency explains the differences in the final morphology of fully covered droplets between CH_4 and CO_2 hydrates (Figure 2). Although Teng *et al.* (1996) hypothesized partial dissociation for CO_2 hydrates, it was Ovalle & Beltran (2021) that first showed this partial dissociation mechanism for propane hydrates and for mixed methane + propane hydrates. Since Figure 3.2 shows partial dissociation for methane, carbon dioxide and their mixtures (structure I formers) and Ovalle & Beltran (2021) observed the same for propane and methane-propane mixtures (structure II formers), it is very possible that growth via partial dissociation is a growth mechanism common to all gas hydrates.

Figure 3.3 shows uniform temperature experiments performed. As mentioned previously, $n\Delta x_g$ was calculated using the solubility of methane for mixtures. All guests formed category one spherulites (Granasy *et al.*, 2005), growing isotropically from a single initial growth point. Carbon dioxide showed feather-like spherulites. Methane and the 80:20 mixture showed similar smooth spherulitic crystal habits and 30:70 presented a coarse, radial crystal habit. Contrary to what was observed at lower driving forces, guests showed different crystal habits, and $n\Delta x_g$ only appeared to correlate morphology of pure CH_4 and the 80:20 mixture.

Figure 3.4 presents experiments at a constant temperature gradient. Driving force in terms of ΔT_{sub} and $n\Delta x_g$ are shown on the sides of each panel. Values of $n\Delta x_g$ shown for mixed hydrates were calculated using methane solubility. All guests show a faceted morphology at low driving forces ($n\Delta x_g \lesssim 5.0$). As the

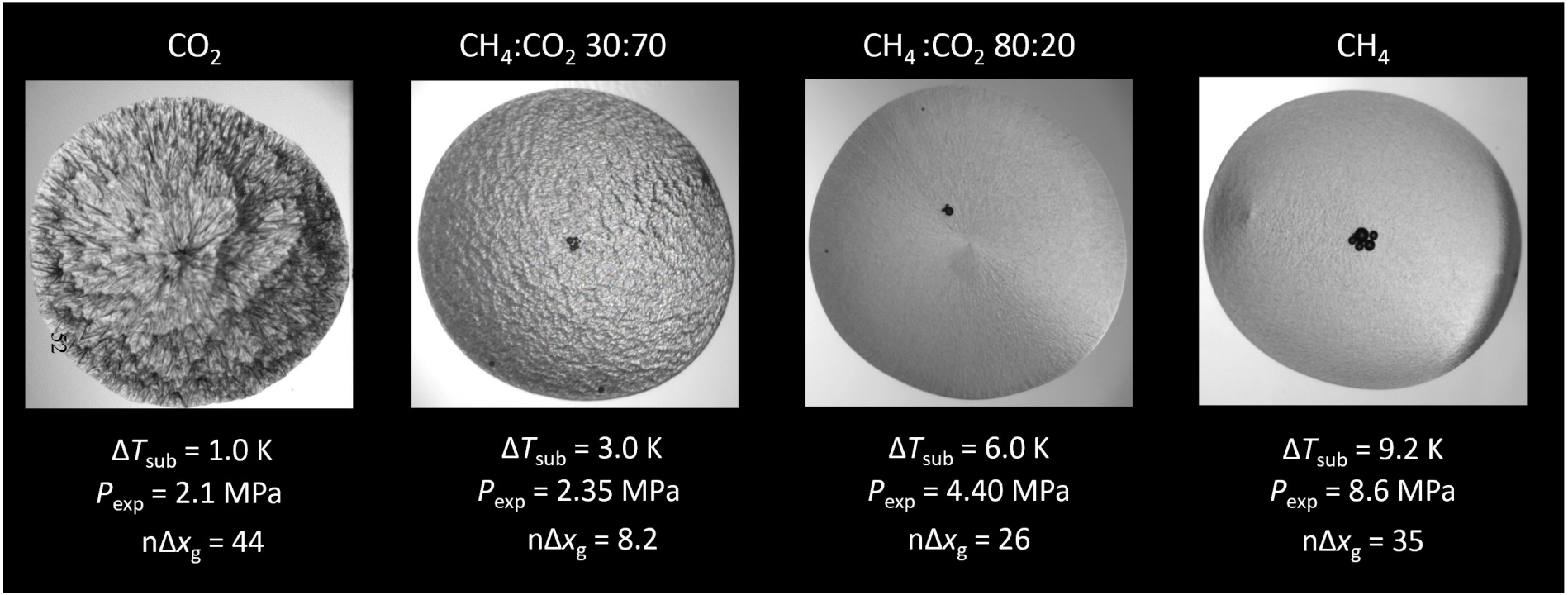

Figure 3.3: Hydrates formed with uniform temperature setting. $n\Delta x_g$ was calculated using the solubility of methane for mixtures. Feed gas composition is specified above each panel. Experimental conditions are shown at the bottom of the figure. CO_2, T_{HLV} = 277.4 K. 30:70, T_{HLV} = 277.4 K. CH_4 T_{HLV} = 284.70. 80:20 T_{HLV} = 280.40.

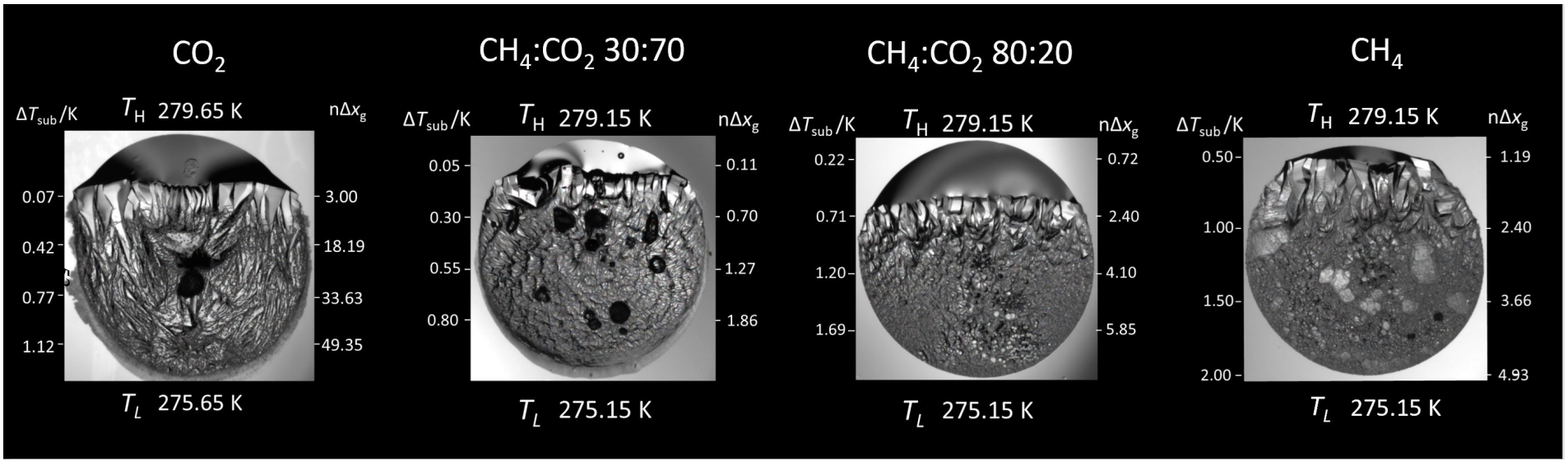

Figure 3.4: Gas hydrates formed at a constant temperature gradient setting. Feed composition is specified above each panel. T_H and T_L are high and low temperatures set on the stage, respectively. CO_2 P_{exp} = 2.10 MPa. CH_4 P_{exp} = 4.0 MPa. 30:70, P_{exp} = 2.35 MPa. 80:20, P_{exp} = 3.25 MPa

driving force increased, an abrupt change in morphology was observed for each guest. Methane and 80:20 changed from faceted to granular morphologies. Large single crystals were formed within the methane hydrate film. Large single crystals have been previously observed in methane hydrates (Li *et al.*, 2013; Duquesnay *et al.*, 2016; Sandoval, 2015). Carbon dioxide transitioned from faceted to needle-like crystal habit and 30:70 changed from faceted to a radial, coarse crystal habit. As $n\Delta x_g$ increases, crystallites decrease their size showing a transition from rougher to flatter habits. Similar changes in morphology have been observed in literature: carbon dioxide, 30:70 and 70:30 mixtures has been observed to change from polyhedra to dendrites while CH_4 transition from faceted to granular with increasing driving force. (Freer *et al.*, 2001; Ohmura *et al.*, 2004; Ueno *et al.*, 2015; Oya *et al.*, 2017; Duquesnay *et al.*, 2016; Beltran & Servio, 2010)

3.1.1 Morphology and growth rates

Figure 3.5 shows gas hydrates formed using a uniform temperature setting graphed versus growth rates. At velocities in the 0.001-0.01 range, morphologies are polyhedral and faceted for all guests. As growth rates increase, morphology changes for each gas mixture. At growth rates above 0.01 mm/s, 80:20 and CH_4 still look similar. These two CH_4-rich guests showed granular morphologies at 0.01 mm/s and smooth spherulites at 0.1 mm/s. In contrast, 30:70 and CO_2 presented unique changes to their crystal habit. Carbon dioxide presented feather-like crystallites in the range of 0.01-0.1 mm/s. The 30:70 gas mixture showed coarse radial morphology past 0.1 mm/s. None of the uniform temperature experiments done during the study resulted in velocities in the 0.01-0.1 mm/s range for 30:70. This change in morphology was also observed on hydrates formed using a temperature gradient (Figure 3.4).

Growth velocity worked as an accurate predictor of morphology for rates under 0.01 mm/s, similar to the extended Kishimoto & Ohmura (2012) model. Nonetheless, correlation with morphology was limited to methane solubility at low driving force ($n\Delta x_g < 2.5$). Using growth rate as a predictor for morphology results advantageous because it is not bound to a specific driving force or hydrate former. Growth rates could be measured and compared using any driving force and any gas mixture. However, growth rates measured with the 3-in-1 technique should be taken as a qualitative measurement of hydrate kinetics. To the best of the author's knowledge, none of the models used to study gas hydrates have been able to represent morphology and kinetics under a single driving force accurately.

In summary, our results resolve the previous apparent discrepancies on the morphology of CH_4 and

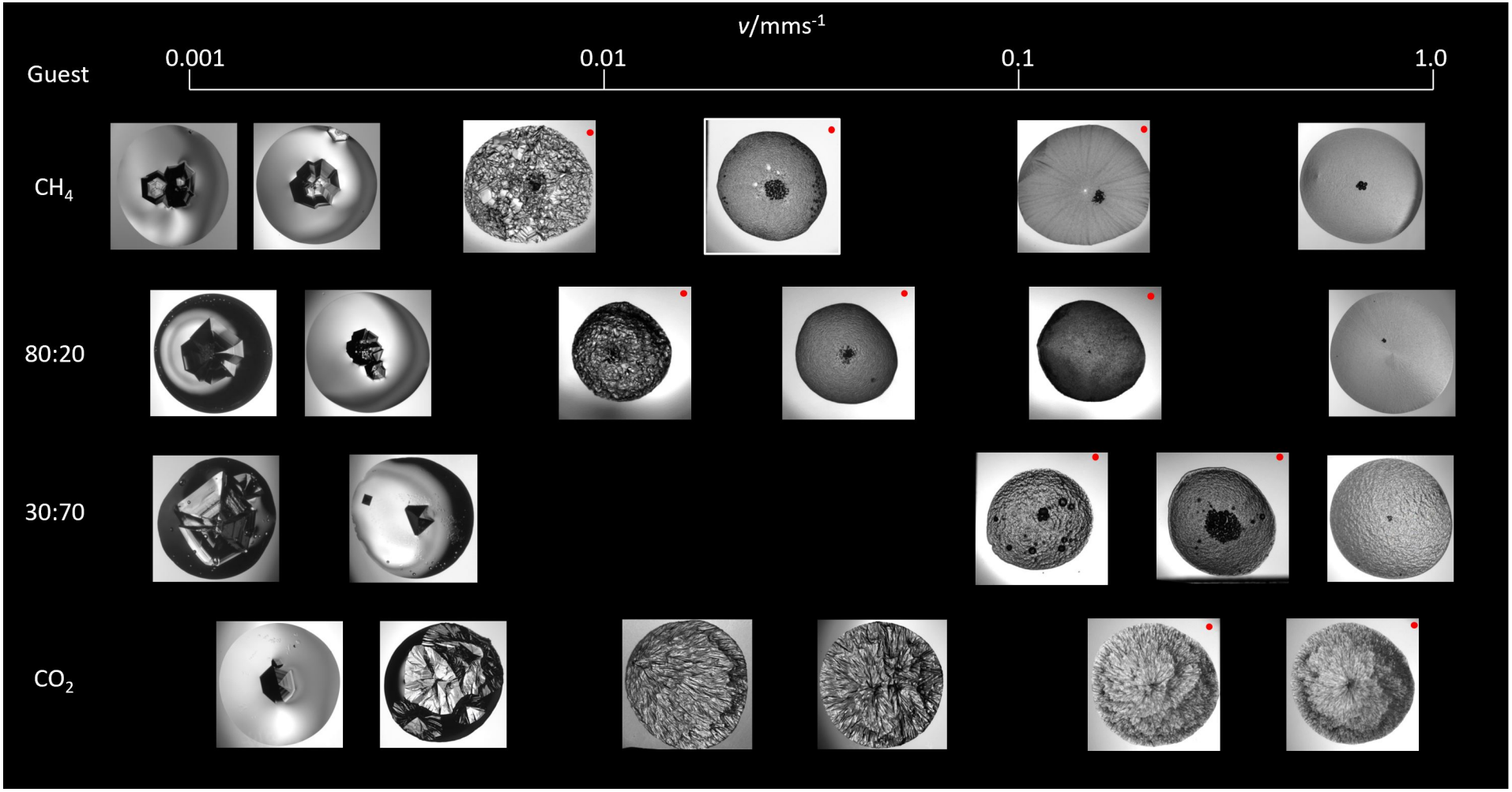

Figure 3.5: Morphology of gas hydrates formed at a uniform temperature. The abscissa shows film growth rates and the ordinate vapor phase composition. Images marked with a red dot were acquired by Ortiz (2018) using the same setup.

CO_2. Regardless of the driving force being used, CH_4, CO_2 and their gas mixtures can exhibit the same crystal habit. Growth rates worked as an accurate qualitative predictor of morphology.

3.2 Growth Velocity

The extended Kishimoto & Ohmura (2012) model proposed in this study only considers the solubility of one component from the feed gas. Thus, $n\Delta x_g$ was calculated using CH_4 first and then CO_2 to show growth rate versus the mass-transfer driving force in terms of each feed component. Growth rate data was evaluated using uniform and constant gradient temperature experiments.

Figure 3.6a (semilog) shows growth rate followed a power-law with respect to $n\Delta x_g$. The mass transfer driving force, $n\Delta x_g$, for the two gas mixtures (80:20 and 30:70) was calculated using solubility of methane. Pure methane and 80:20 data tracked each other closely, while the 30:70 mixture velocity appeared to be approximately one order of magnitude higher than that of pure methane above $n\Delta x_g \sim 2$. Carbon dioxide presented lower growth rates than all other the hydrate formers studied.

Figure 3.6b shows the correlation low driving forces ($n\Delta x_g < 2.0$) of both gas mixtures with pure methane growth rates. Notably, under a $n\Delta x_g$ of 1.5, growth rates fall within the 0.001-0.01 mm/s range where morphologies resemble each other (Figure 3.5).

Pure methane and the 80:20 mixture growth rates followed the same trend at all values of $n\Delta x_g$. These two hydrate formers also showed similar morphologies across all driving forces (Figures 3.5 and 3.4). It is possible that the different trends of growth rates indicate why at low $n\Delta x_g$, all hydrates formed comparable morphologies, while the two guests, which follow a unique trend, formed different crystal habits at higher driving forces.

The mass transfer driving force, $n\Delta x_g$, was also calculated using CO_2 mole fractions (Figure 3.7). Figure 3.7a shows growth rates in a semilogarithmic scale versus $n\Delta x_g$ of all hydrate formers in this study. In this case, methane presents higher growth rates than all other guests when compared at equal $n\Delta x_g$. At low driving forces ($n\Delta x_g < 25$), 80:20 growth velocity is higher than 30:70 at the same $n\Delta x_g$. Once the mass transfer driving force increase passed $n\Delta x_g = 25$, 30:70 shows higher growth rates than 80:20.

As shown on Figure 3.7b, $n\Delta x_g$ of the two gas mixtures seem to track pure CO_2 at low driving forces ($n\Delta x_g < 15$). Growth rates corresponding to $n\Delta x_g \leqslant 15$ on this graph are under 0.01 mm/s. These driving forces presented similar morphologies for all guests. At $n\Delta x_g \geqslant 20$, both gas mixtures growth velocities diverged considerably from those of pure CO_2.

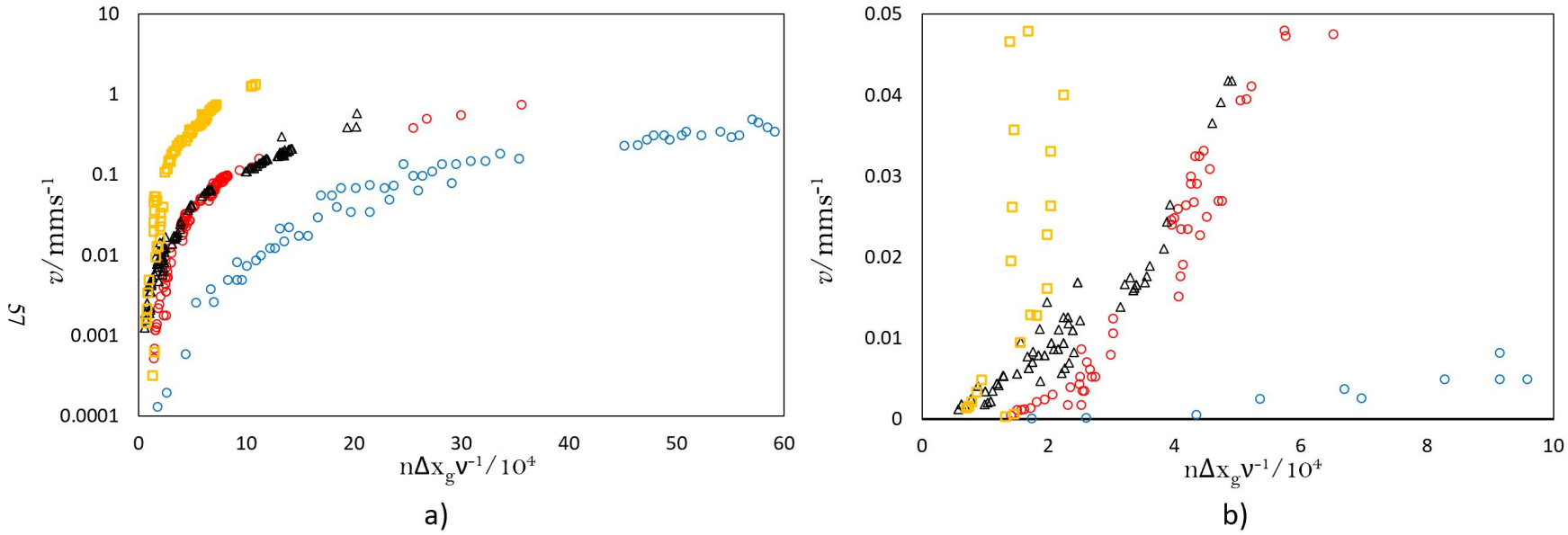

Figure 3.6: Hydrate film growth versus difference in solubility ($n\Delta x_g$) of CH_4, CO_2, 80:20 and 30:70 hydrates. Values of $n\Delta x_g$ for the two mixtures was calculated using solubility of methane. Data from Ortiz (2018) and Sandoval (2015) was used in this graph. ○, CO_2. ○, CH_4. □, 30:70. △, 80:20.

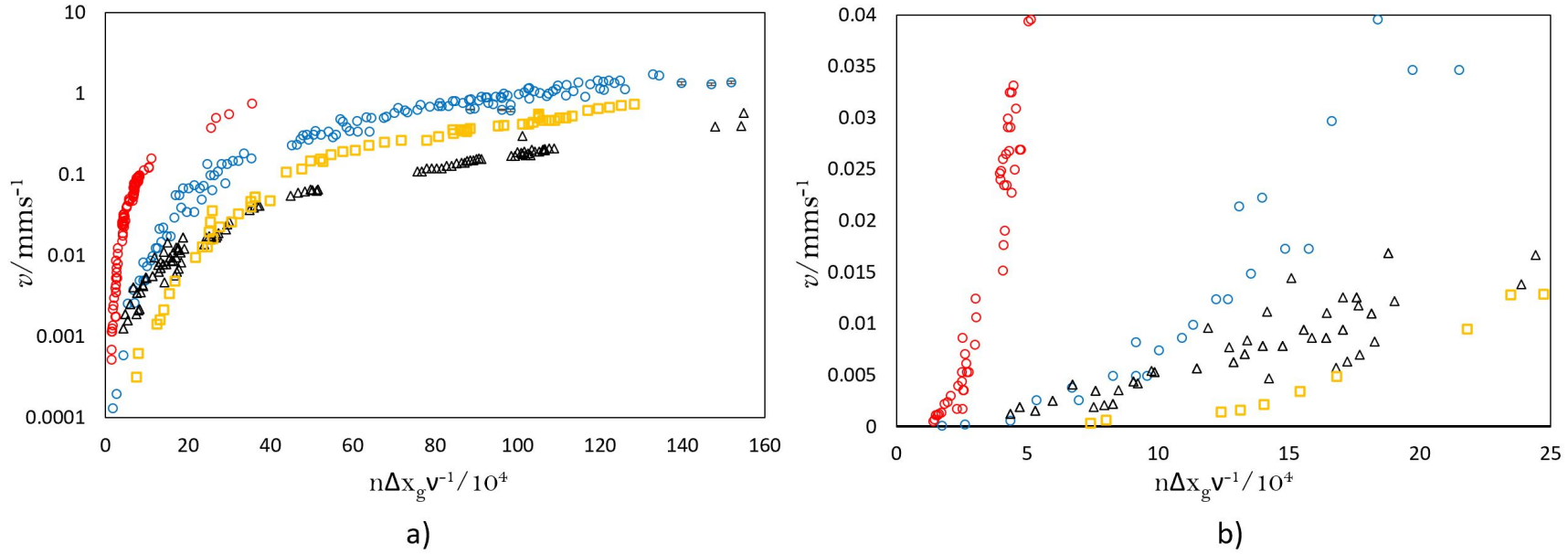

Figure 3.7: Hydrate film growth versus difference in solubility ($n\Delta x_g$) of CH_4, CO_2, 80:20 and 30:70 hydrates. $n\Delta x_g$ of 80:20 and 30:70 were found using solubility of CO_2. Data from Ortiz (2018) and Sandoval (2015) was used in this graph. o, CO_2. o, CH_4. □, 30:70. Δ, 80:20.

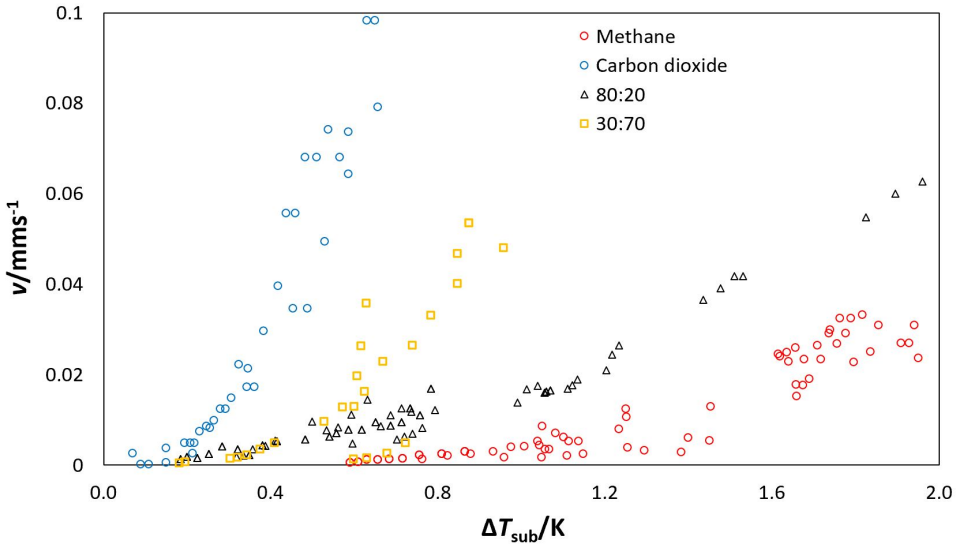

Figure 3.8: Hydrate film growth versus difference subcooling of CH_4, CO_2, 80:20 and 30:70 hydrates. Data from Ortiz (2018) and Sandoval (2015) was used in this graph. ○, CO_2. ○, CH_4. □, 30:70. △, 80:20.

Figure 3.8 shows growth rate data versus ΔT_{sub} from Ortiz (2018) and Sandoval (2015). It can clearly be seen that at the same ΔT_{sub}, growth rates of methane and carbon dioxide were very different. However, for film growth velocities v $\leqslant$ 0.01 mm/s, nΔx_g seemed to follow the same trend as that of the pure guest used to find the difference in solubility (Fig 3.6b for CH_4 or Fig 3.7b for CO_2). In addition, below this growth v $\leqslant$ 0.01 mm/s, morphology also matched across guests (Figure 3.5). Thus, we propose that nΔx_g provides and adequate indicator for morphology at low growth velocities.

One possible interpretation for the success of our extended Kishimoto & Ohmura (2012) model could be based on Englezos *et al.* (1987b)'s idea, where enclathration of each component is not affected by the presence of the other gas. The overall consumption of gas is the sum of each component's individual rate of consumption in the mixture. Thus, these graphs (Figure 3.6 and 3.7) of growth rate versus $n\Delta x_g$ provide a good representation of the relationship between driving force and apparent kinetics at low driving forces ($n\Delta x_g \lesssim 3.0$ on Figure 3.6b, $n\Delta x_g \lesssim 15$ on Figure 3.7b).

At the same $n\Delta x_g$, CO_2 presented lower growth rates than methane. This could be the result of differing intrinsic rates. Recent studies show that the intrinsic growth rate of CO_2 is about four times lower than CH_4 (Bergeron & Servio, 2008; Bergeron *et al.*, 2010). When the growth rates of these two guests were compared using ΔT_{sub}, CO_2 growth rates are considerably faster(Peng *et al.*, 2007; Ortiz, 2018; Sandoval, 2015). At ΔT_{sub} = 1 K, CO_2 has a $n\Delta x_g$ of 45 while CH_4's is 2.4. Thus, our extended mass transfer model

appears to offer a better qualitative representation of intrinsic than the heat transfer model.

Overall, the kinetics and growth mechanism of mixed CH_4:CO_2 hydrates are not fully understood. Studies using analytical techniques have shown that methane is preferentially consumed during early stages of CH_4:CO_2 hydrate formation. (Lang & Servio, 2018; Schicks & Luzi-Helbing, 2013; Horvat *et al.*, 2012). Studies using Raman spectra have shown that small cages of structure I, which are occupied preferentially by CH_4, are formed before any enclathration of CO_2 occurred. Schicks & Luzi-Helbing (2015) stated that this early formation of CH_4 hydrates hinders the enclathration of CO_2 into the hydrate phase. Furthermore, it has been proposed that the formation of these binary hydrates is controlled by the competition between the two guests for occupancy of structure I large cages (Uchida *et al.*, 2005). Uchida *et al.* (2005) stated that the preferential enclathration of CH_4 at early stages occurred for mixtures with a lower CH_4/CO_2 molar ratio than 0.3. The CH_4/CO_2 ratio for our CO_2 rich mixture (30:70) is 0.43. In other words, methane could be acting as a rate-limiting guest for CO_2 enclathration. In this work, the presence of methane in both the 80:20 and 30:70 mixtures slowed growth velocity (in terms of CO_2) at the same $n\Delta x_g$ compared to pure carbon dioxide (Figure 3.7a).

Our results at low velocities (v $\leqslant$ 0.01 mm/s) seem to agree with the theoretical models proposed by Englezos *et al.* (1987b) and Skovborg & Rasmussen (1994) where the enclathration of each component in the gas phase is not affected by the presence of other guests. However, both the analytical methods in the literature and our own results at higher velocities seem to point to the need for a model that accounts for the interaction between the components in the feed gas.

3.2.1 Growth velocity and morphology

Figures 3.9 to 3.12 show hydrate-film growth rates plotted against nΔx_g (Figures3.9 to 3.12, "a" panels), alongside images of hydrates formed under a temperature gradient (Figures 3.9 to 3.12, "b" panels). The mass transfer driving force, nΔx_g, was calculated using methane mole fractions. Plots of growth rates of pure methane and the 80:20 and 30:70 mixtures presented two inflection points in terms of nΔx_g: methane growth rates showed inflection points at nΔx_g = 3 and nΔx_g = 7 (Figure 3.9); the 80:20 mixture exhibited inflection points at nΔx_g = 4 and nΔx_g = 10; and the 30:70 mixture's inflection points were found at nΔx_g = 0.9 and nΔx_g = 2. These are approximate values. Only one sharp change in growth rates was clearly visible for CO2 at nΔx_g = 18, approximately. The first inflection point in the growth rate of each guest coincided with an abrupt change in morphology from polyhedral to smooth on hydrates formed with a temperature

gradient (Figure 3.9b-3.12b).

These changes in morphology can be explained by the growth mechanisms that correspond to each driving force (Sunagawa, 2005) (Figure 1.15). At low driving forces, polyhedral crystals bounded by flat faces are expected. As the driving force increases, the growth mechanism changes to two-dimensional growth and then adhesive growth. This change in mechanism is reflected on the changes in morphology and growth rates, where abrupt changes were observed.

Figure 3.5 shows how morphology of each guest changes with increasing growth rates. The graph clearly shows three types of morphology as described by Sunagawa (2005). At low velocities (v < 0.01 mm/s), polyhedral crystals can be observed for all mixtures. At intermediate velocities ($0.01 \lesssim v \lesssim 0.1$ mm/s) granular habits develop for methane and the mixtures, whereas CO_2 shows feather-like growth. Finally above, v > 0.1 mm/s spherulites are observed.

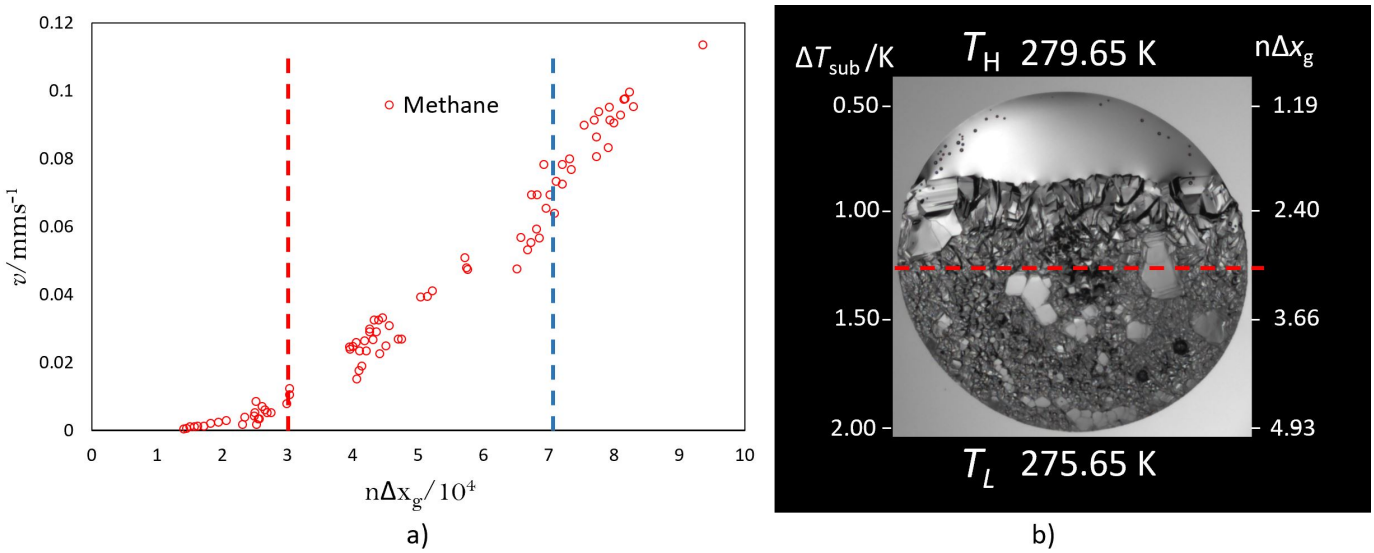

Figure 3.9: Growth rates graphed versus $n\Delta x_g$ and CH_4 hydrates formed under a constant temperature gradient. The red and blue dotted lines indicate inflection points in growth rate with respect to $n\Delta x_g$. The first inflection in growth rate corresponds to an abrupt change in morphology. Growth rate data from Sandoval (2015) and Ortiz (2018) was used.

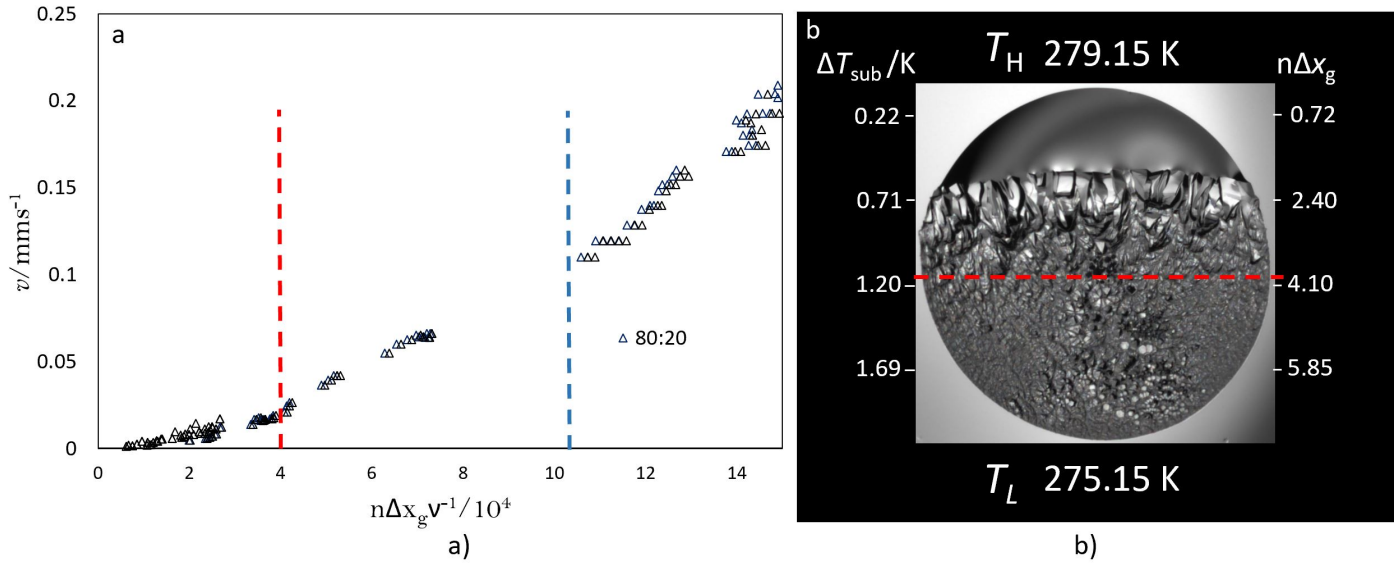

Figure 3.10: Growth rates graphed versus $n\Delta x_g$ and 80:20 hydrates formed under a constant temperature gradient. The red and blue dotted lines indicate inflection points in growth rate with respect to $n\Delta x_g$. The first inflection in growth rate corresponds to an abrupt change in morphology. Growth rate data from Ortiz (2018) was used.

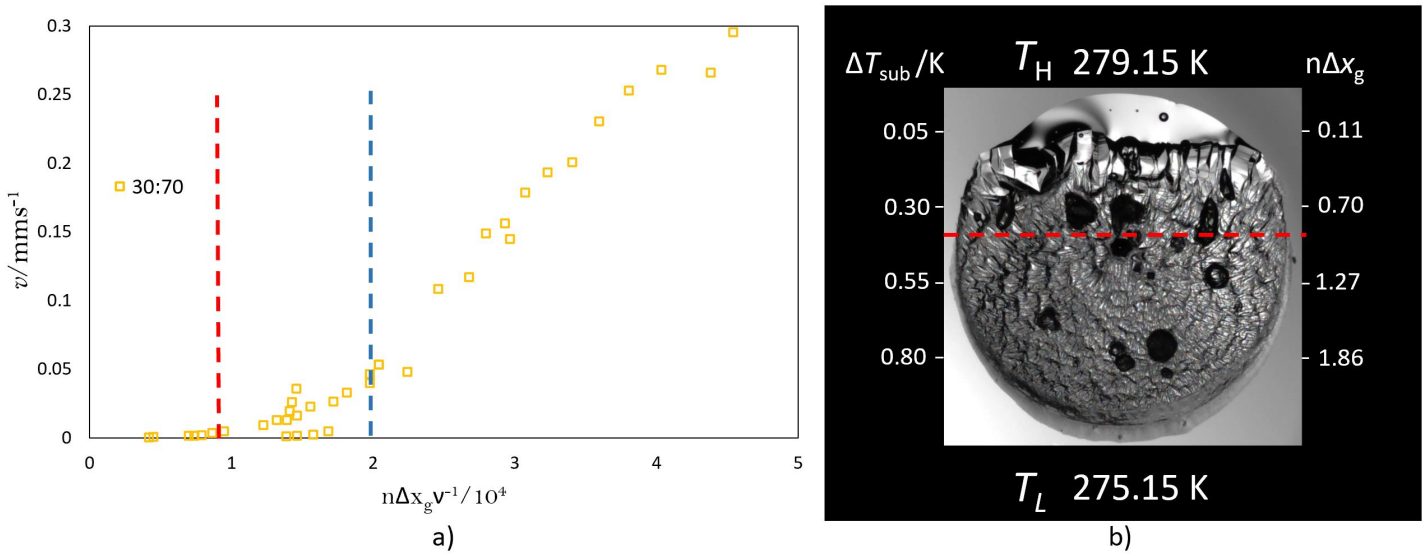

Figure 3.11: Growth rates graphed versus nΔx_g and 30:70 hydrates formed under a constant temperature gradient. The red and blue dotted lines indicate inflection points in growth rate with respect to nΔx_g. The first inflection in growth rate corresponds to an abrupt change in morphology. Growth rate data from Ortiz (2018) was used.

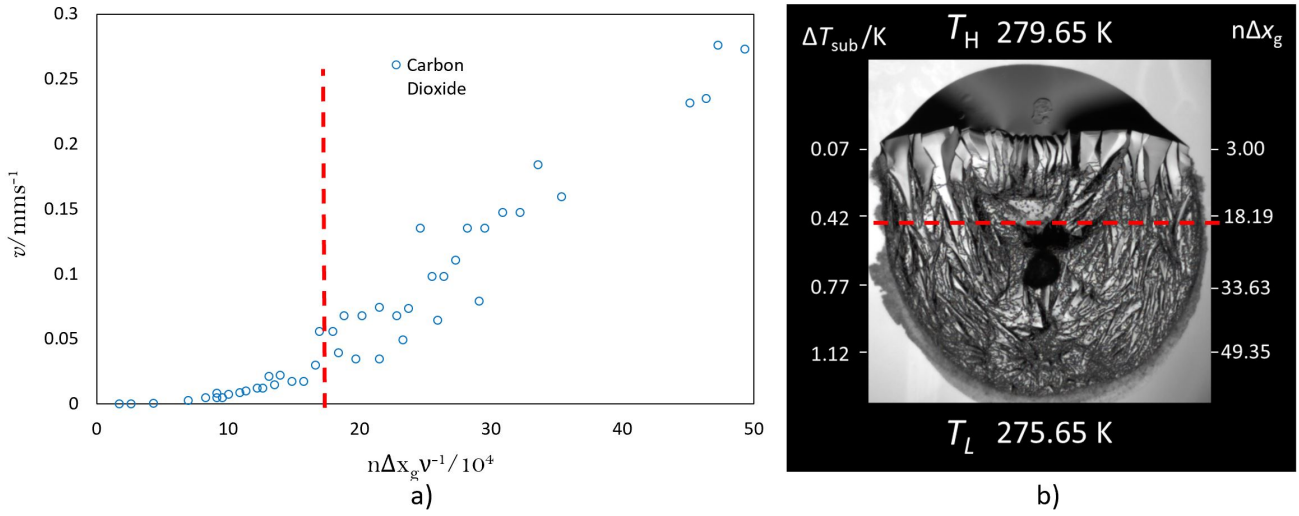

Figure 3.12: Growth rates graphed versus nΔx_g and CO_2 hydrates formed under a constant temperature gradient. The red and blue dotted lines indicate inflection points in growth rate with respect to nΔx_g. The first inflection in growth rate corresponds to an abrupt change in morphology. Growth rate data from Sandoval (2015) and Ortiz (2018) was used.

Chapter 4

Conclusions

This work used the 3-in-1 technique to study morphology, kinetics and growth mechanism of methane, carbon dioxide and two of their mixtures (CH_4:CO_2, 80:20 and 30:70 nominal concentration).

Previous apparent contradictions in literature were resolved. Methane and carbon dioxide and two mixtures can exhibit the same crystal habit. All guests formed euhedral, faceted morphologies at growth rates under 0.01 mm/s. However, at $v \geqslant 0.01$ mm/s different crystal habits were observed for each guest. Carbon dioxide exhibited feather-like crystal habits, 30:70 presented a coarse radial morphology. Methane and 80:20 formed similar smooth morphologies. We determined that growth rates are an accurate qualitative predictor of morphology for all guests at $v \leqslant 0.01$ mm/s.

Hydrates formed from all gases in this study showed partial dissociation during growth. To the best of the author's knowledge, this is the first time partial dissociation is shown for methane, carbon dioxide and their mixtures.

The mass-transfer model proposed by Kishimoto & Ohmura (2012) was extended for gas mixtures. Our extension of this model used the liquid-phase mole fraction of one component in the feed gas to measure the driving force ($n\Delta x_g$). Overall, growth rates for the 80:20 and 30:70 mixtures followed the trend of the pure component used to find $n\Delta x_g$ at low driving forces. The 80:20 mixture closely tracked methane growth rates for $n\Delta x_g$ calculated with methane mole-fractions. Notably, the morphology of all guests were similar within values of $n\Delta x_g$ where growth rates tracked each other. Overall, our extension for mixtures of Kishimoto & Ohmura (2012)'s model worked as a qualitative predictor of morphology and growth rates at low driving forces ($n\Delta x_g \lesssim 5.0$). None of these predictive qualities were observed in previous studies using ΔT_{sub} as

the driving force.

As driving force ($n\Delta x_g$) increased, growth rates and morphology for all guests exhibited sharp changes in growth rate as driving force increased. The 3-in-1 technique allowed us to observe changes in morphology on a single experiments using a temperature gradient. Changes in the crystal and growth velocity with increasing driving force were evidence of a change in the growth mechanism for crystals.

4.1 Future Work

- Perform additional uniform temperature experiments for the 30:70 CH_4+CO_2 mixture in order to fully understand the changes in morphology between 0.01 to 0.1 mm/s growth rates.
- Study morphology, growth rates and growth mechanism of other structure I formers such as ethane and methane+ethane mixtures. Characterizing other structure I formers could give more insights into the growth mechanism and morphology of structure I hydrates overall.
- Use our extension of Kishimoto & Ohmura (2012)'s model with a 50:50 CH_4+CO_2 mixture in order to further study the role of methane as a rate-limiting guest of carbon dioxide enclathration as well as the effect of composition in morphology of binary hydrates.
- Study structure II hydrate formers and mixtures using Kishimoto & Ohmura (2012)'s model and our extension for mixtures.
- Apply the 3-in-1 technique to study kinetics, morphology and phase equilibrium of ternary mixtures. Our extension of Kishimoto & Ohmura (2012)'s model could be of use to understand the kinetics and morphology of these mixtures.

Bibliography

B. P. McGrail, H. T. Schaef, M. D. White T. Zhu A. S. Kulkami R. B. Hunter S. L. Patil A. T. Owen P F. Martin. 2007. *Using Carbon Dioxideto Enhance Recovery of Methane from Gas Hydrate Reservoirs: FinalSummary Report*. Tech. rept. U.S. Department of Energy.

Belandria, Veronica, Eslamimanesh, Ali, Mohammadi, Amir H., Theveneau, Pascal, Legendre, Herve, & Richon, Dominique. 2011. Compositional Analysis and Hydrate Dissociation Conditions Measurements for Carbon Dioxide + Methane + Water System. *Industrial & Engineering Chemistry Research*, **50**(9), 5783–5794.

Beltran, J.G, & Servio, P. 2008. Equilibrium Studies for the System Methane + Carbon Dioxide + Neohexane + Water. *Journal of Chemical Engineering Data*, **53**, 1745–1749.

Beltran, J.G., & Servio, P. 2010. Morphological Investigations of Methane-Hydrate Films Formed on a Glass Surface. *Journal of Crystal Growth and Design*, **10**, 4339–4347.

Beltran, J.G., Bruusgaard, H., & Servio, P. 2012. Gas hydrate phase equilibria measurement techniques and phase rule considerations. *Journal of Chemical Thermodynamics*, **22**, 1–4.

Bergeron, S., & Servio, P. 2008. Reaction Rate Constant of CO_2 Hydrate Formation and Verification of Old Premises Pertaining to Hydrate Growth Kinetics. *AIChE Journal*, **54**, 2964–2970.

Bergeron, S., Beltran, J.G., & Servio, P. 2010. Reaction rate constant of methane clathrate formation. *Fuel*, **89**, 294–301.

Daniel-David, D., Guerton, F., Dicharry, C., Torre, J., & Broseta, D. 2015. Hydrate growth at the interface between water and pure or mixed CO_2/CH_4 gases: influence of pressure,temperature, gas composition and water-soluble surfactants. *Chemical Engineering Science*, **132**, 118–127.

Davy, H. 1811. The Bakerian Lecture: On Some of the Combinations of Oxymuriatic Gas and Oxygene, and on the Chemical Relations of These Principles, to Inflammable Bodies. *Philossophical Transactions of the Royal Society of London*, **101**, 1–35.

Decarie, G., & Beltran, J.G. 2011. Effect of hydrate guest on clathrate morphology. *In: Proceedings of the 7th International Conference on Gas Hydrates. Edinburgh, Scotland, United Kingdom, July 17-21*.

Decarie, Gina. 2012. *A COMPARATIVE STUDY ON THE MORPHOLOGY AND GROWTHRATES OF CARBON DIOXIDE AND METHANE HYDRATES*. M.Phil. thesis, Royal Military College of Canada.

Duquesnay, J.R., Diaz Posada, M.C., & Beltran, J.G. 2016. Novel gas hydrate reactor design: 3-in-1 assessment of phase equilibria, morphology and kinetics. *Fluid Phase Equilibria*, **413**, 148–157.

Englezos, P. 1993a. Clathrate Hydrates. *Industrial and Engineering Chemistry Research*, **32**, 1251–1274.

Englezos, P., Kalogerakis, N., Dholabhai, P. D., & Bishnoi, P. R. 1987a. Kinetics of formation of methane and ethane gas hydrates. *Chemical Engineering Science*, **42**, 2647–2658.

Englezos, P., Kalogerakis, N., Dholabhai, P. D., & Bishnoi, P. R. 1987b. Kinetics of gas hydrate formation from mixtures of methane and ethane. *Chemical Engineering Science*, **42**, 2659–2666.

Englezos, Peter. 1993b. Clathrate hydrates. *Industrial & Engineering Chemistry Research*, **32**(7), 1251–1274.

Fogg, P., & Gerrard, W. 1991. *Solubility of Gases in Liquids: A Critical Evaluation of Gas/Liquid Systems in Theory and Practice*. Wiley.

Freer, E. M., Selim, M. S., & Sloan, E. D. 2001. Methane hydrate film growth kinetics. *Fluid phase equilibria*, **185**, 65–75.

Gong, Deyu, Huang, Shipeng, Wu, Wei, Yu, Cong, Fang, Chenchen, & Liu, Dan. 2014. Characteristics of Gas Compositions in Giant Gas Fields of China. *Energy Exploration & Exploitation*, **32**(4), 635–656.

Granasy, L., Pusztai, T., G., Tegze, Warren, J.A., & Douglas, J.F. 2005. Growth and form of spherulites. *Physical Review E*, **72**, 011605.

Hammerschmidt, E. G. 1934. Formation of gas hydrates in natural gas transmission lines. *Industrial and Engineering Chemistry Fundamentals*, **26**, 851–855.

Hashemi, S., Macchi, A., Bergeron, S., & Servio, P. 2006. Prediction of methane and carbon dioxide solubility in water in the presence of hydrate. *Fluid phase equilibria*, **246**, 131–136.

Herri, J.-M., Bouchemoua, A., Kwaterski, M., Fezoua, A., Ouabbas, Y., & Cameirao, A. 2011. Gas hydrate equilibria for CO2–N2 and CO2–CH4 gas mixtures—Experimental studies and thermodynamic modelling. *Fluid Phase Equilibria*, **301**(2), 171–190.

Horvat, Kristine, Kerkar, Prasad, Jones, Keith, & Mahajan, Devinder. 2012. Kinetics of the Formation and Dissociation of Gas Hydrates from CO2-CH4 Mixtures. *Energies*, **5**(7), 2248–2262.

Kang, Seong-Pil, & Lee, Huen. 2000. Recovery of CO2from Flue Gas Using Gas Hydrate: Thermodynamic Verification through Phase Equilibrium Measurements. *Environmental Science & Technology*, **34**(20), 4397–4400.

Katz, Donald L. 1971. Depths to Which Frozen Gas Fields (Gas Hydrates) May Be Expected. *Journal of Petroleum Technology*, **23**(04), 419–423.

Kidnay, A. J. 2020. *Fundamentals of natural gas processing*. Place of publication not identified: CRC Press.

Kishimoto, M., & Ohmura, R. 2012. Correlation of the Growth Rate of the Hydrate Layer at a Guest/Liquid-Water Interface to Mass Transfer Resistance. *Energies*, **5**, 92–100.

Kitamura, M., & Mori, Y. 2013. Clathrate-hydrate film growth growth along water/methane phase boundaries–and observational study. *Crystal Research and Technology*, **48**, 511–519.

Koh, Carolyn A., Sloan, E. Dendy, Sum, Amadeu K., & Wu, David T. 2011. Fundamentals and Applications of Gas Hydrates. *Annual Review of Chemical and Biomolecular Engineering*, **2**(1), 237–257.

Lang, Francis, & Servio, Phillip. 2018. Bulk liquid and gas mole fraction measurements during hydrate growth for the CH+ CO2+ H2O system. *The Journal of Chemical Thermodynamics*, **117**(feb), 113–118.

Li, S., Sun, C, Liu, B., Li, B., Chen, G., & Sum, A. 2014. New Observations and Insights into the Morphology and Growth Kinetics of Hydrate Film. *Scientific Reports*, **4**, 4129.

Li, Sheng-Li, Sun, Chang-Yu, Liu, Bei, Feng, Xiu-Jun, Li, Feng-Guang, Chen, Li-Tao, & Chen, Guang-Jin. 2013. Initial thickness measurements and insights into crystal growth of methane hydrate film. *AIChE Journal*, **59**(6), 2145–2154.

Lu, Hailong, taek Seo, Yu, won Lee, Jong, Moudrakovski, Igor, Ripmeester, John A., Chapman, N. Ross, Coffin, Richard B., Gardner, Graeme, & Pohlman, John. 2007. Complex gas hydrate from the Cascadia margin. *Nature*, **445**(7125), 303–306.

Mak, Thomas C. W., & McMullan, Richard K. 1965. Polyhedral Clathrate Hydrates. X. Structure of the Double Hydrate of Tetrahydrofuran and Hydrogen Sulfide. *The Journal of Chemical Physics*, **42**(8), 2732–2737.

Mullin, J. W. 2001. *Crystallization*. Elsevier.

Ohmura, R., Shimada, W., Uchida, T., Mori, Y.H., Takeya, S., Nagao, J., Minagawa, H., Ebinuma, T., & Narita, H. 2004. Clathrate hydrate crystal growth in liquid water saturated with a hydrate-forming subtance: variations in crystal morphology. *Philosophical Magazine*, **84**, 1–16.

Ohmura, R., Matsuda, S., Uchida, T., Ebinuma, T., & Narita, H. 2005. Clathrate Hydrate Crystal Growth in Liquid Water Saturated with a Guest Substance: Observations in a Methane + Water System. *Crystal Growth and Design*, **5**, 953–957.

Ortiz, Nathalia. 2018. *3-in-1 technique applied to mixed CH4:CO2 gas hydrates*. M.Phil. thesis, Universidad de los Andes.

Ovalle, Sebastian, & Beltran, Juan G. 2021. Growth Mechanisms and Phase Equilibria of Propane and Methane + Propane Hydrates. *Journal of Chemical & Engineering Data*, jun.

Oya, Shun, Aifaa, Muhammad, & Ohmura, Ryo. 2017. Formation, growth and sintering of CO 2 hydrate crystals in liquid water with continuous CO 2 supply: Implication for subsurface CO 2 sequestration. *International Journal of Greenhouse Gas Control*, **63**(aug), 386–391.

Peng, B., Dandekar, A., Sun, C., Luo, H., Ma, Q., Pang, W., & Chen, G. 2007. Hydrate Film Growth on the Surface of a Gas Bubble Suspended in Water. *Journal of Physical Chemistry B*, **111**, 12485–12493.

Perrin, Andrea, Musa, Osama M., & Steed, Jonathan W. 2013. The chemistry of low dosage clathrate hydrate inhibitors. *Chemical Society Reviews*, **42**(5), 1996.

Ripmeester, J. A., Tse, J. S., Ratcliff, C. I., & Powell, B. M. 1987. A new clathrate hydrate structure. *Nature*, **325**, 135–136.

Saito, K., Sum, A., & Ohmura, R. 2010. Correlation of Hydrate-Film Growth Rate at the Guest/Liquid-Water Interface to Mass Transfer Resistance. *Industrial and Engineering Chemistry Research*, **49**, 7102–7103.

Sandoval, Juan Felipe. 2015. *A Comparative Study On the Growth Mechanism, Kinetics and Morphology of Carbon Dioxide and Methane Hydrates*. M.Phil. thesis, Universidad de los Andes.

Schicks, Judith M., & Luzi-Helbing, Manja. 2013. Cage occupancy and structural changes during hydrate formation from initial stages to resulting hydrate phase. *Spectrochimica Acta Part A: Molecular and Biomolecular Spectroscopy*, **115**(nov), 528–536.

Schicks, Judith M., & Luzi-Helbing, Manja. 2015. Kinetic and Thermodynamic aspects of Clathrate Hydrate Nucleation and growth. *Journal of Chemical Engineering Data*, **60**, 269–277.

Servio, P., & Englezos, P. 2003. Morphology of Methane and Carbon Dioxide Hydrates Formed from Water Droplets. *AIChE Journal*, **49**, 269–276.

Skovborg, P., & Rasmussen, P. 1994. A mass transport limited model for the growth of methane and ethane gas hydrates. *Chemical Engineering Science*, **49**, 1131–1143.

Sloan, E. D., & Koh, C. A. 2008. *Clathrate Hydrates of Natural Gases*. 3rd edn. Chemical Industries. CRC Press.

Smelik, E. A., & King, H. E. 1997. Crystal-growth studies of natural gas clathrate hydrates using a pressurizes optical cell. *American Mineralogist*, **82**, 88–98.

Smith, J., H., Van Ness, & M., Abott. 2001. *Introduction to Chemical Engineering Thermodynamics*. McGraw-Hill.

Subramanian, S. Sloan, E. D. 2002. Solubility Effects on Growth and Dissolution of Methane Hydrate Needles. *In: Proceedings of the fourth International Conference on Gas Hydrates*.

Sum, Amadeu K., Koh, Carolyn A., & Sloan, E. Dendy. 2012. Developing a Comprehensive Understanding and Model of Hydrate in Multiphase Flow: From Laboratory Measurements to Field Applications. *Energy & Fuels*, **26**(7), 4046–4052.

Sunagawa, Ichiro. 2005. *Crystals : growth, morphology, and perfection*. Cambridge: Cambridge University Press.

Tanaka, R., Sakemoto, R., & Ohmura, R. 2009a. Crystal Growth of Clathrate Hydrates Formed at the Interface of Liquid Water and Gaseous Methane, Ethane, or Propane: Variations in Crystal Morphology. *Crystal Growth and Design*, **9**, 2529–2536.

Tanaka, Ryo, Sakemoto, Riki, & Ohmura, Ryo. 2009b. Crystal Growth of Clathrate Hydrates Formed at the Interface of Liquid Water and Gaseous Methane, Ethane, or Propane: Variations in Crystal Morphology. *Crystal Growth & Design*, **9**(5), 2529–2536.

Teng, H., Yamasaki, A., & Shindo, Y. 1996. Stability of the hydrate layer formed on the surface of a CO2 droplet in high-pressure, low-temperature water. *Chemical Engineering Science*, **51**(22), 4979–4986.

Trebble, M. A., & Bishnoi, P. R. 1987. Development of a new equation of state. *Fluid phase equilibria*, **35**, 1–18.

Uchida, T., Ebinuma, T., Kawabata, J., & Narita, H. 1999. Microscopic observations of formation processes of clathrate-hydrate films at an interface between water and carbon dioxide. *Journal of Crystal Growth*, **204**, 348–356.

Uchida, T., Ikeda, M., Takeya, S., Kamata, Y., Ohmura, R., Nagao, J., Zatsepina, O. Y., & Buffet, B. A. 2005. Kinetics and Stability of CH4 -CO_2 Mixed Gas Hydrates during Formation and Long-Term Storage. *ChemPhysChem*, **6**, 646–654.

Ueno, H., Akiba, H., Akatsu, S., & Ohmura, R. 2015. Crystal growth of clathrate hydrates formed with methane + carbon dioxide mixed gas at the gas/liquid interface and in liquid water. *New Journal of Chemistry*, **39**, 8254–8262.

Vysniauskas, A., & Bishnoi, P. R. 1983. A kinetic study of methane hydrate formation. *Chemical Engineering Science*, **38**, 1061–1972.

Copyright

Table 4.1: Copyright statements of figures used in this publication

Figure	Copyright statement
Figure 1.1	Republished with permission of Annual Reviews, from Fundamentals and Applications of Gas Hydrates, Koh et al., Vol. 2:237-257, 2010; permission conveyed through Copyright Clearance Center, Inc.
Figures 1.6, 1.7, 1.15	Reproduced from Crystals Growth, Morphology, & Perfection, Ichiro Sunagawa, 2005 with permission of Cambridge University Press through PLSclear.
Figure 1.9 , 1.17, 1.18	Reprinted from Chemical Engineering Science, Volume 132, Delphine Daniel-David, Fabrice Guerton, Christophe Dicharry, Jean-Philippe Torre, Daniel Broseta, 18 August 2015, Pages 118-127, copyright 2015, with permission from Elsevier.
Figure 1.10	Republished with permission of Elsevier Science & Technology Journals, from Cage occupancy and structural changes during hydrate formation from initial stages to resulting hydrate phase, Judith M Schicks, Manja Luzi-Helbing, 115, 528-536, copyright 2013; permission conveyed through Copyright Clearance Center, Inc.
Figure 1.14	Republished with permission of Elsevier Science & Technology Journals, from Crystallization, J.W. Mullin, fourth edition, copyright 2001; permission conveyed through Copyright Clearance Center, Inc.
Figure 1.16	Republished with permission of John Wiley and Sons, from Peter Englezos and Phillip Servio, Morphology of methane and carbon dioxide hydrates formed from water droplets, Copyright 2003, American Institute of Chemical Engineers (AIChE).
Figure 1.17	Reprinted (adapted) with permission from Morphological Investigations of Methane Hydrate Films Formed on a Glass Surface, Juan G. Beltrán, Phillip Servio, Crystal Growth and Design. Copyright 2010 American Chemical Society.
Figure 1.17	Reprinted (adapted) with permission from Hydrate Film Growth on the Surface of a Gas Bubble Suspended in Water, Peng et al., The Journal of Physical Chemistry B. Copyright 2007 American Chemical Society.